Chemical flux analysis of low-temperature plasma-enhanced oxidation of methane and hydrogen in argon

Combustion and Flame 257 (2023) 113037

Contents lists available at ScienceDirect

Combustion and Flame

journal homepage: www.elsevier.com/locate/combustflame

Chemical flux analysis of low-temperature plasma-enhanced oxidation of methane and hydrogen in argon

T. Hazenberg[a,*], J. van Dijk[b], J.A. van Oijen[a]

[a] Mechanical Engineering, Eindhoven University of Technology, PO box 513, MB Eindhoven 5600, The Netherlands
[b] Applied Physics, Eindhoven University of Technology, PO box 513, MB Eindhoven 5600, The Netherlands

ARTICLE INFO

Article history:
Received 19 April 2023
Revised 11 August 2023
Accepted 20 August 2023

Keywords:
Plasma-assisted combustion
Low-temperature chemistry
Plasma chemistry
Hydrogen
Methane
Mechanism

ABSTRACT

Plasma can be used to enhance the reactivity of combustible mixtures at low temperatures. In this article, the chemical pathways predicted by three different reaction mechanisms are investigated for the low-temperature oxidation of hydrogen and methane. To validate our model and the reaction mechanisms, the numerical results are compared against experimental results in a diluted flow reactor. Our model with all three reaction mechanisms predicts trends similar to those observed in the experiments. Moreover, all predicted quantities show reasonable quantitative agreement with the experiments. Flux analysis is used to identify the main pathways of oxidation at different temperatures. Three different modes, each active in a different temperature range, are identified in the oxidation of hydrogen. When the temperature is increased, these modes become increasingly self-sustained. Similarly, three different pathways are identified in the oxidation of methane. Below 1000K, methane quickly removes hydroxyl radicals from the radical pool, inhibiting self-sustained oxidation. From our analysis, we conclude that plasma provides activation of the low-temperature chemistry by the generation of radicals.

1. Introduction

Plasma-assisted combustion (PAC), has been researched extensively in the past decades as a promising method for reliable ignition and flame stabilization in challenging conditions [1–7]. Plasmas can enhance ignition and flame stability via thermal, kinetic and transport pathways [5,6]. Even though numerous articles have been published [8–13], no consensus has been reached on the importance of these pathways [11,13]. For the activation of combustion chemistry, non-equilibrium plasmas are considered to be interesting. These types of discharges are characterized by a high electron energy and relatively low gas temperature. These high-energy electrons are hypothesized to efficiently dissociate fuel and oxygen, producing initial combustion radicals [5,6]. A popular method for generating a strong non-equilibrium plasma is via nanosecond repetitively pulsed dielectric barrier discharges, e.g. [14–22]. Because dielectric barrier discharges allow for the creation of a strong non-equilibrium plasma, while also providing control over the energy deposition. Even though numerous works have investigated plasma-assisted combustion, no consensus has been reached on the mechanism by which plasma enhances combustion [3,5].

A major challenge in the predictive modeling of PAC is the development of a reliable plasma and low-temperature oxidation chemistry [4–6]. Many authors have developed detailed chemical models for plasma in several bath gasses [23–26]. When researching PAC chemistry, it is required to combine one of these plasma chemistries with a combustion mechanism, e.g. [14,16,17,27–31]. Then, several new reactions have to be introduced to capture the interaction of electronically excited states and conventional combustion species. These electronically excited states are created by the plasma and carry significant potential energy, which significantly accelerates the reaction rate of reactions in which they participate. Due to its large popularity, some authors opt to use GRI-Mech 3.0 [32] as the base combustion mechanism [27–29]. However, it is worth noting that the last release of GRI-Mech 3.0 has been more than 20 years ago. Significant progress in understanding hydrocarbon oxidation has been made since then, especially in the low-temperature regime. Moreover, none of the optimization targets used to develop GRI-Mech 3.0 are ignition experiments below 1300K. This raises the question about the validity of the oxidation pathways in GRI-Mech 3.0 at low temperatures, as it was not developed for these conditions. To be clear, we are not questioning

* Corresponding author.
E-mail address: t.hazenberg@tue.nl (T. Hazenberg).

https://doi.org/10.1016/j.combustflame.2023.113037

the validity of GRI-Mech 3.0 in conventional applications, as it has proven itself as a relatively small but reliable mechanism.

Since the release of GRI-Mech 3.0, significant advances have been made to improve our understanding of low-temperature oxidation. This has led to the development of several new mechanisms, some popular examples are AramcoMech 2.0 [33–35] and HP-mech [36,37]. The Aramco mechanism is developed over a series of articles in a hierarchical fashion. First, the combustion chemistry of H_2 and CO is modeled [33], which is then extended with the combustion of methane, methanol, etc. [34]. The result is a very detailed mechanism that is validated for a wide array of fuels and conditions. These conditions include flow reactor experiments down to 600K, i.e., temperatures relevant to plasma-assisted combustion. Especially at low temperatures, AramcoMech is found superior compared to GRI-Mech 3.0 [38,39]. HP-mech has been used in fewer published research works but has been validated for plasma-assisted combustion research, e.g., [16,17,40].

The ability of plasma to rapidly dissociate molecules at low temperatures, allows them to activate reactions at low temperatures. Exactly this chemistry activation is one of the main difficulties in low-temperature oxidation experiments. Therefore, plasma-assisted oxidation experiments can provide unique insight into low-temperature oxidation pathways. In a series of papers, Tsolas et al. [18,19,41] and Togai et al. [42] performed measurements of plasma-assisted oxidation in a flow reactor setup. The flow reactor experiments are conducted in a highly diluted Argon (Ar > 99% vol) environment. These diluted conditions are ideal to study the kinetics of plasma-assisted combustion at a constant temperature, as the chemical heat release is negligible. Due to the negligible heat release, thermo-chemical plasma instabilities are avoided [43,44], which makes it possible to generate a rather uniform plasma. Though in [45] a 0D model gave reasonable results for filamentary plasma, we studied oxidation in a nearly homogenous plasma to remove as many uncertainties as possible. Zero-dimensional models are ideal to study plasma kinetics as these are sufficiently affordable to utilize detailed chemical mechanisms.

Performing plasma-assisted oxidation experiments in diluted conditions does have its limitations, as the bath gas has an inevitable effect on the plasma chemistry [46]. This implies that in the experiments of Tsolas et al. [18,19,41] and Togai et al. [42] the plasma chemistry is driven by argon. As such, the chemistry in these experiments is mostly driven by dissociative quenching of electronically excited argon, producing conventional combustion radicals. Similarly, in the experiments of Snoeckx et al. [30], where an extremely lean ($\phi = 0.01$) oxygen/hydrogen mixture is oxidized, the electronically excited oxygen chemistry is dominant. In contrast, in a follow-up study [31] where an extremely rich ($\phi = 49.5$) oxygen/hydrogen mixture is used, the chemistry is dominated by hydrogen radicals. At the same time we should realize that the chemical potential associated with an electronically excited state is lost within a couple of reactions and conventional radicals are formed, e.g., [7,30,31,42,47], these radicals then take part in the low-temperature oxidation chemistry. Therefore, different bath gasses are required to study the plasma chemistry, but the low-temperature oxidation chemistry studied under diluted conditions can to a large extent be generalized.

In this article, we develop a thermodynamically consistent [48] plasma chemistry mechanism. This mechanism is coupled with three different combustion mechanisms (GRI-Mech 3.0, AramcoMech 2.0 and HP-mech). The mechanisms are time-integrated with a 0D equivalent circuit model. This equivalent circuit model is used to describe nanosecond dielectric barrier discharges. These numerical results are compared to the measurements performed by Tsolas et al. [18,19,41] and Togai et al. [42]. Since GRI-Mech 3.0 is not developed for larger hydrocarbons, only the oxidation of H_2 and CH_4 is considered. All mechanisms predict similar trends as observed in the experiments, but (significant) quantitative differences are present. The main differences to earlier numerical work in this setup [42,47,49], is our sensitivity analysis on model parameters and our more detailed flux analysis. In this analysis, the temperature dependence of different pathways is studied in detail. From this analysis, we conclude that plasma can induce sustained reactivity in H_2 and not in CH_4 below the ignition threshold. With sustained reactivity, we mean: significant reactivity (or continuation of the oxidation) in the combustible mixture after plasma activation.

2. Method

In this article, a flow reactor is modeled as used in the experiments of Tsolas et al. [18,19]. The reactor is heated to a certain temperature with a fixed flow of a highly diluted combustible mixture blue($X_{Ar} > 0.99$). At the entry of the reactor, a DBD is placed which provides plasma activation. We will assume that this is a spatially homogenous plasma. After this plasma, the flow remains at a constant temperature for some time before it is cooled. We assume that the mixture does not react further while it is being cooled and stop our simulations at the end of the constant temperature section. At the exhaust of the flow reactor, gas samples are captured and analyzed using a gas analyzer. It is assumed that convective fluxes are much larger than diffusive fluxes and therefore the entire reactor can be modeled as a plug-flow reactor.

2.1. Governing equations

A zero-dimensional plug-flow reactor at constant pressure p and temperature T, which has a density ρ is modeled. The position inside the flow reactor x can be related to time t by assuming that the flow velocity v is constant:

$$\mathrm{d}x = v\mathrm{d}t. \tag{1}$$

For the flow velocity to be constant, the density changes must be negligible. This is reasonable, as the energy deposition and chemical heat release is low, such that the temperature is (nearly) constant [19,41]. Togai et al. [49] modeled this reactor both as a constant temperature reactor and an adiabatic reactor. They found that the temperature rise is less than 35K in the adiabatic case and should therefore not impact the results. Additionally, due to the diluted conditions, the changes in composition are only minor. Using the transformation from Eq. 1 the conservation equations are written in terms of time instead of reactor position. The species mass fractions, Y_i, for N_s species are computed via the conservation of species:

$$\rho\frac{\mathrm{d}Y_i}{\mathrm{d}t} = \omega_i M_i \quad \text{for} \quad i = 1, N_s, \tag{2}$$

where ω_i is the chemical source term (mol/m^{3}s) and M_i is the molar mass of species i.

One of the main challenges in 0D plasma modeling is estimating the deposited energy and reduced electric field. To model this, we employ an equivalent circuit model [49,50]. The dielectric barrier discharge is modeled as a capacitor (C_d) and the gas as a capacitor (C_g) and a variable resistor (R_g) in parallel, see Fig. 1. When the applied voltage $V_p(t)$ increases, a voltage drop over the discharge gap is created, i.e., an electric field is induced. This electric field accelerates free electrons in the gas, which results in chemical activation and ionization of the gas. When electrical breakdown of the gas occurs (electron concentration is high) the resistance of the variable resistor R_g reduces significantly. In a short time, a large current, the conductive current (i_{cond}), runs through the gas providing most of the coupled energy. This current short circuits the gas-phase capacitor and quickly charges the dielectric capacitor. Due to the charging of the dielectric capacitor, the voltage drop

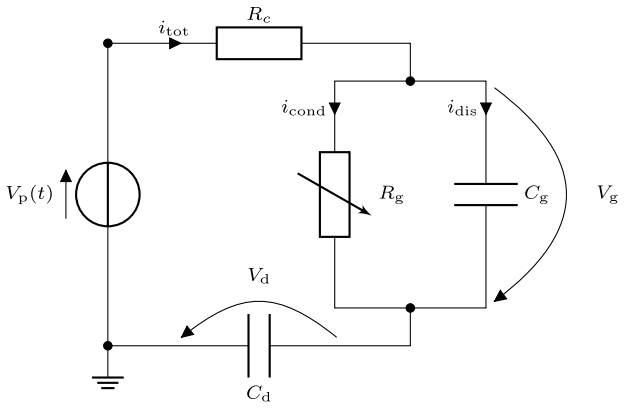

Fig. 1. A schematic representation of the equivalent circuit model employed.

across the discharge gap reduces, which removes the electric field in the discharge gap. Finally, the cable resistance is modeled as an Ohmic resistor (R_c). In our further discussion, we have used the naming convention as presented in for example Pai et al. [51] and Rusterholtz et al. [52]. This model has as input $V_p(t)$ and the dielectric constants: C_d and C_g. The dielectric constants are dependent on the experimental setup, which will be discussed later.

A set of algebraic differential equations is then solved to obtain the plasma power. The voltage drop across the dielectric, V_d, evolves as a function of the total current, i_{tot}, via

$$C_d \frac{dV_d}{dt} = i_{tot}. \tag{3}$$

Next, the voltage drop across the discharge gap (V_g) is given by

$$C_g \frac{dV_g}{dt} = i_{tot} - i_{cond}. \tag{4}$$

The displacement current, i.e., the current charging the gas phase capacitor is given by $i_{dis} = i_{tot} - i_{cond}$. To close this system of equations, conservation of current through a cable resistor is used,

$$i_{tot} + \frac{V_p(t) - V_d - V_g}{R_c} = 0. \tag{5}$$

In this equation (t) is used to indicate that V_p is a user-defined time-dependent function, while V_d and V_g are solved via Eq. 3 and Eq. 4. Eq. 5 is an algebraic equation, which balances the actual i_{tot} with that expected based on the voltage drop across the resistor. The advantage of this formulation compared to the formulation by Togai [49], is that this formulation ensures the conservation of current. Moreover, the applied voltage is used instead of its derivative, which provides two advantages:

1. The derivative of the applied voltage is not required, which allows for much more arbitrary voltage waveforms
2. Numerical integration of a derivative can result in a drift of V_p, which is avoided in this formulation.

The entire set of $N_s + 2$ differential Eqs (2,3 and 4) and 1 algebraic Eq. (5) is solved using Sundials IDA solver [53,54].

2.2. Closure

The ideal gas law is utilized to relate molar concentration to pressure and temperature:

$$c = \frac{p}{RT}. \tag{6}$$

Similarly, the density is computed as

$$\rho = \frac{p\bar{M}}{RT}, \tag{7}$$

with $\bar{M}$ the mean molar mass of the mixture.

For the chemical source term (ω_i), consider a general chemical reaction

$$\sum_{i=1}^{N_s} \nu'_{k,i}\chi_i \leftrightarrow \sum_{i=1}^{N_s} \nu''_{k,i}\chi_i, \tag{8}$$

where $\nu'_{k,i}$ and $\nu''_{k,i}$ are the forward and reverse stoichiometric coefficients for species i in reaction k and χ_i the symbol for species i. The rate-of-progress for this reaction is then given by:

$$R_k = \prod_{i=1}^{N_s} k_{f,i} c_i^{\nu'_{k,i}} - \prod_{i=1}^{N_s} k_{b,i} c_i^{\nu''_{k,i}}, \tag{9}$$

where $k_{f,i}$ and $k_{b,i}$ are the forward and reverse rate constant following Chemkin [55] and c_i is the molar concentration of species i ($c_i = \rho Y_i / M_i$). The chemical source term of species i is then obtained via

$$\omega_i = \sum_{k=1}^{N_r} (\nu''_{k,i} - \nu'_{k,i}) R_k. \tag{10}$$

Additional plasma-based reactions are added to the conventional Chemkin rate constants. These plasma-based reactions involve electrons, whose reaction rate is dependent on the electron energy distribution function (EEDF). The electrons can have a significantly different kinetic energy (temperature) than the gas, as these are easily accelerated by the electric field. As such, the kinetic energy of the electrons is determined by the reduced electric field (E/N, with $N = cN_a$). Rate constants of reactions involving electrons are therefore a function of the reduced electric field and the gas composition. In the cases of interest, the mixture composition does not change drastically, such that the composition dependency is negligible. Therefore, these rate constants are pre-computed using the two-term Boltzmann solver Bolsig [56] and tabulated as a function of E/N for use during the simulation. In the Supplementary Materials results are presented where this table is updated every five discharges to validate this assumption.

The reduced electric field (Vm^2) inside the discharge gap is computed via

$$E/N = \frac{|V_g|}{d_{gap} c N_A}, \tag{11}$$

with d_{gap} the discharge gap height and N_A Avogadro's constant. The gas-phase current i_{cond} can then be computed using the electron mobility, μ_e,

$$i_{cond} = c_e \mu_e E A_{gap}, \tag{12}$$

where A_{gap} is the area of the discharge gap. Just as the rates of reaction for reactions involving electrons, the electron mobility is a function of the reduced electric field and the gas composition. Therefore, it is also tabulated and retrieved during the simulation.

2.3. Reaction mechanisms

The chemistry used in this article is based on the work of [29]. However, several modifications are made: First, the thermodynamic data of excited state species is corrected as outlined in Hazenberg et al. [48]. Second, as the thermodynamic data of excited state species is now consistent, reverse rates of reactions with excited state species are computed from thermodynamic principles. Third, the argon plasma chemistry is extended based on the mechanism provided by Tsolas [57]. The rate of dissociative dissociation of Ar^* with H_2 and O_2 used by Tsolas et al. is close to recent measurements by Winters et al. [20]. Fourth, three different combustion mechanisms are used: 1) GRI-Mech 3.0 [32] as originally done in [29], 2) HP-mech [36,37] which is developed for low-temperature kinetics and 3) AramcoMech 2.0 [33–35] which also

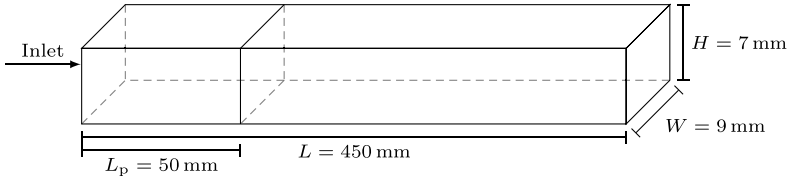

Fig. 2. Schematic of the experimental setup with key dimensions [18,19].

includes a more detailed low-temperature description. Fifth, the list of electron/neutral collisions is extended; now it involves Ar, O_2, H_2, CH_4, O_3 and H_2O. The cross sections for these processes are taken from LXCat [58], where Ar, O_2 and H_2 cross sections come from the IST-Lisbon database [59], the CH_4 set comes from Bouwman et al. [60] (which is an extension of Song et al. [61]) and the O_3 and H_2O come from the Morgan database [62]. The authors realize that the H_2O dataset from Morgan should not be used in Bolsig, as it does not include rotational processes. However, the conditions of interest contain more than 99 %vol Argon. As such, the overall electron-to-gas energy transfer and EEDF are predominantly determined by the Ar cross sections. Therefore, neglecting the rotational energy transfer does not (significantly) impact the overall transfer, while electron dissociation, like

$$H_2O + e \rightarrow H + OH + e, \tag{R.1}$$

is included in this manner. As a word of caution, this invalidates the mechanism in the presence of significant water vapor concentration. All three mechanisms are provided in the Supplementary Materials, including the tabulation of the electron reaction rate constants.

3. Validation of model and mechanisms

3.1. Experimental setup

We validate our methodology and mechanism against the constant temperature flow reactor experiments from Tsolas and Togai [18,19,41,42,49]. For a detailed description of the experimental conditions and the setup dimensions, we refer the reader to those articles. Here is a summary: A gas mixture flows through a 45cm (L) long duct with a rectangular cross section at isothermal conditions, of which the first 5cm (L_p) can be treated by the plasma. At the outlet of the reactor, the gas composition is measured with a gas analyzer. The height of the discharge gap is 7mm (d_gap) and the width of the reactor is 9mm (W). The area of the discharge gap, required in Eq. 12, is then $A_\mathrm{gap} = WL_\mathrm{p}$ Within this discharge area, nanosecond discharges are generated by a DBD setup with a frequency of 1kHz. In Fig. 2, a schematic is provided of these setup dimension.

The coupled plasma power is determined by the maximum voltage ($\max(V_\mathrm{p}(t)) = 10\mathrm{kV}$), the pulse rise-time and the dielectric constants in the equivalent circuit model [63]. These parameters are estimated as follows: Using the parallel plate capacitor formula and the setup parameters we estimate $C_\mathrm{g} = 0.57\mathrm{pF}$ and $C_\mathrm{d} = 4.05\mathrm{pF}$. The uncertainty of these parameters is relatively large, the reason for which is twofold: 1) The uncertainty of the dielectric constant of the involved materials is large. 2) The fact that the discharge gap size is large compared to the width of the reactor means that the parallel plate formula is strictly not applicable. Unfortunately, no coupled power measurements are available. Therefore, these estimated parameters can not be validated. Though the cable resistance (R_c) has a physical meaning, we have mainly included it in the model to provide closure of the governing equations and improve numerical stability. For these simulations, we have used $R_\mathrm{c} = 1\mathrm{m}\Omega$ such that the results are not modified by it while maintaining numerical stability. The low value for R_c is equivalent to assuming that the voltage waveform is measured near the DBD instead of at the power supply. The voltage waveform is obtained by fitting a Weibull function to the waveform provided by Togai et al. [49].

The temperature of the isothermal region is modified from 405 to 1260K, while the pressure is constant at 1atm. In each of these experiments, the volume flow rate (at standard conditions) is identical such that the residence time (τ) inside the reactor reduces with temperature ($\tau = 510.3\mathrm{Ks}/T$ and $\tau_\mathrm{p} = 56.7\mathrm{Ks}/T$) [49]. As a result, τ_p varies from 140 to 45ms and thus the number of plasma discharges received by the mixture varies between 140 and 45. Simulations can only be performed for an integer number of discharges. This implies that it is only possible to simulate at discrete values of the residence time, and thus discrete reactor temperatures. Therefore, the rector temperature is increased in steps. The temperature difference between two simulations can then be obtained from

$$\Delta T = 56.7e3\frac{\Delta N_\mathrm{p}}{(N_\mathrm{p} - \Delta N_\mathrm{p})N_\mathrm{p}}, \tag{13}$$

where N_p is the number of discharges received by the mixture and ΔN_p is the difference in the number of discharges between simulations. Near the ignition temperature, we have performed simulations at every integer number of discharges, while below the ignition threshold, we have performed simulations for every five discharges.

3.2. Electrical characteristics

To validate our equivalent circuit model we have performed a simulation in pure Ar. The simulation is performed at 1atm and 600K with a peak voltage of 9.8kV, these values are taken from Tsolas et al. [64]. Only in this simulation, a peak voltage of 9.8kV is used, which matches the value provided by Tsolas et al. [64] while earlier works report 10kV [18,19,42,49]. In the left frame of Fig. 3, the applied voltage waveform and voltage across the discharge gap are presented. The applied voltages are obtained from Tsolas et al. [64] by converting the electric field, assuming a peak voltage of 9.8kV. The discharge gap voltage is obtained by assuming a gap size of 7mm. A comparison is made between the present V_p and the model and measurement of Tsolas et al. [64]. The only difference between the present voltage waveform and that presented in Tsolas et al., is that we used a Weibull function, while Tsolas et al. used a Gaussian function. Both waveforms closely match the experimentally measured waveform.

When comparing the voltage waveforms across the discharge gap between our work and the model results of [64], some differences and similarities can be observed. In both, the present results and the results from Tsolas et al. the voltage drop across the discharge gap increases until $t \approx 100\mathrm{ns}$. The increase in the voltage has a similar shape as the voltage provided by the power supply. In both, the voltage drop across the discharge gap is slightly lower than that delivered by the power supply, which is due to the capacitance of the dielectric material. At approximately 100ns electrical breakdown occurs, which can be seen from the sharp decrease in the discharge gap voltage. Breakdown occurs because the electron concentration in the gap is sufficiently large such that the

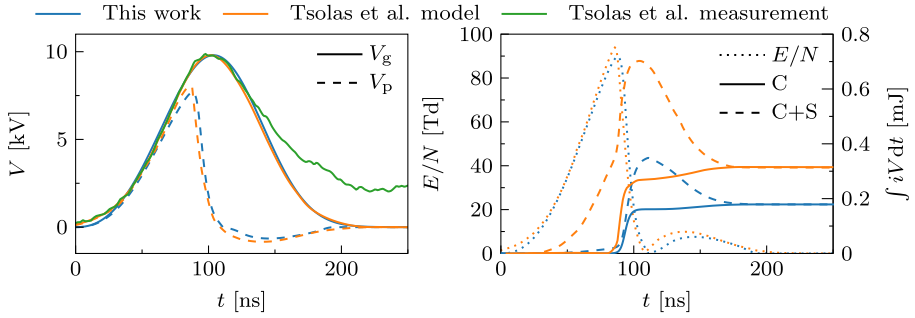

Fig. 3. Left) Applied voltage waveform (V_p) and voltage across the discharge gap (V_g). Right) reduced electric field in the discharge gap (left axis), the coupled energy (right axis) and the coupled + stored energy (right axis). All for a single discharge in pure Ar at 1atm and 600K. In blue is our modeling effort, in orange is the model result presented in Tsolas et al. [64] and in green the power supply measurement by Tsolas et al. [64]. (For interpretation of the references to colour in this figure legend, the reader is referred to the web version of this article.)

gas becomes conductive. Electrical charge quickly accumulates on the dielectric material, opposing the applied voltage and thereby reducing the gap voltage. In the results of Tsolas et al., electrical breakdown of the discharge gap occurs slightly earlier and at a slightly higher voltage. The small difference in gap voltage at breakdown explains the difference in peak E/N, shown in the right graph.

After the peak in applied voltage, the voltage in the discharge gap becomes negative. As a result, the charge accumulated at the dielectric material returns via the conductive channel back to the power supply. In this second discharge (reflected pulse), some amount of energy is coupled into the plasma at a low reduced electric field, see the right frame of Fig. 3. The energy deposited in the discharge gap (coupled energy) and the energy deposited in the discharge gap plus the energy stored in the dielectric capacitor (coupled + stored energy) are also included in the right graph. The coupled energy is computed by integrating $i_{\mathrm{cond}}V_g$, while the coupled + stored energy is computed by integrating $i_{\mathrm{tot}}V_p(t)$. Note that the energy lost in the cable resistance R_c is negligible due to its low resistance. Two notable differences can be identified by comparing our modeling results to those in Tsolas et al. [64]: 1) The stored energy before breakdown occurs is much larger in Tsolas et al. than in the present results. This implies that the total circuit capacitance ($C_{\mathrm{tot}}^{-1} = C_{\mathrm{d}}^{-1} + C_{\mathrm{g}}^{-1}$) is much larger in their results. 2) The final coupled energy is larger in the results of Tsolas et al. than in our results. This is most likely the result of a larger C_{d} in their model. As a consequence, more charge is transferred during breakdown and thus during the reflected pulse, which leads to a higher coupled energy.

The deposited energy is an important parameter in plasma-assisted oxidation/combustion as it directly determines how many excited species can be produced. Unfortunately, no measurements are available for the deposited energy in this experimental setup. Tsolas et al. [64] do provide an estimate for the energy loading obtained in two different ways: 1) estimation of the coupled energy via the model of Adamovich et al. [63] (referred to as model) and 2) estimation of the coupled energy by matching the fuel consumption (ethylene) (referred to as inferred). In our model, the energy loading is computed by integrating $i_{\mathrm{cond}}V_g$ over the duration of the simulation. Within our framework the coupled energy is computed for the entire range temperature range of the experiments [18,19,41,42,49] and three mixtures:

1. Mixture of $X_{\mathrm{Ar}} = 0.995$, $X_{\mathrm{O_2}} = 3000$ppm and $X_{\mathrm{H_2}} = 2000$ppm
2. Mixture of $X_{\mathrm{Ar}} = 0.9954$, $X_{\mathrm{O_2}} = 3000$ppm and $X_{\mathrm{CH_4}} = 1600$ppm
3. $X_{\mathrm{Ar}} = 1$

The coupled energy is computed for all three mechanisms and is found to be nearly identical ($< 0.5\%$).

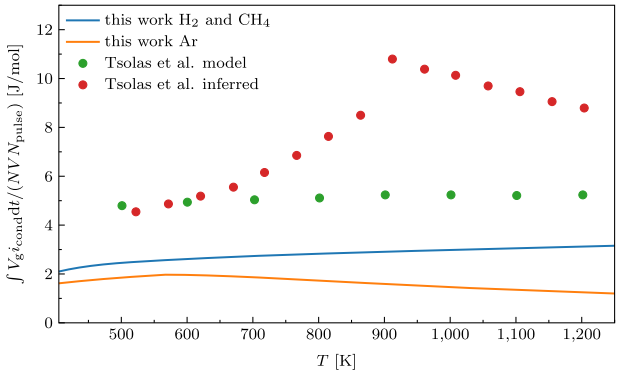

Fig. 4. Energy loading in joule of coupled energy per pulse per mole of gas. The energy loading is computed for: 1) the H_2 (see Section 3.3) and CH_4 (see Section 3.4) experiments, drawn with a single line as these are nearly identical. 2) pure Ar, 3) the model and 4) inferred results presented in Tsolas et al. [64].

In Fig. 4 the energy loading in joule per mole per pulse is compared to those presented in Tsolas et al. [64]. The energy loading of the $H_2/O_2/Ar$ and $CH_4/O_2/Ar$ cases very less than 2.5% over the entire temperature range and are therefore drawn as a single line. The model and inferred values provided by Tsolas et al. are significantly higher than those predicted by our methodology. All modeling results indicate that the coupled energy is rather constant with temperature, which is expected [63]. Several noteworthy observations can be made:

1. Our modeling results predict that the energy loading does depend on the gas composition even in these diluted conditions. The dependence on gas composition is due to electron attachment reactions against oxygen. Electron attachment reactions are very fast and can thus modify the electron concentration even if $X_{\mathrm{O_2}}$ is only 3000ppm.
2. Our modeling results are roughly half those predicted by the model in Tsolas et al. [64]. This is most likely due to different estimates of the dielectric capacitance.
3. The inferred results in Tsolas et al. are more than two times higher than the model results. Moreover, these results are a strong function of temperature.

The large difference in estimates for the coupled energy is not that surprising: 1) Dielectric constants for the materials used are uncertain and 2) the parallel plate formula does not include edge effects. It might very well be that the dielectric constants are a factor two higher. In Table 1 we have reported the coupled energy at $T = 630$K for different model parameters. The top row contains the default parameters, both C_{d} and C_{g} have been doubled and for completeness, a physically accurate value for R_c is also included.

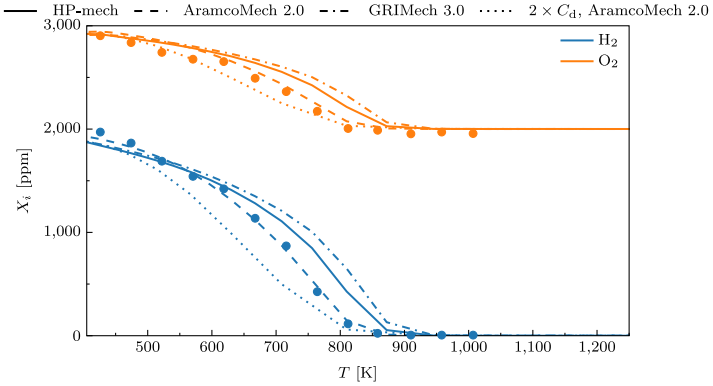

Fig. 5. Mole fractions of H_2 and O_2 as a function of reactor temperature, initial molar fractions are: $X_{Ar} = 0.995$, $X_{O_2} = 3000$ppm and $X_{H_2} = 2000$ppm. The solid lines are results obtained with HP-mech, dashed with AramcoMech 2.0, dash-dot with GRI-Mech 3.0, symbols are (measurements) from [19] and dotted AramcoMech 2.0 with twice the default C_d value.

Table 1
Discharge energy for different model parameter in the plasma-assisted oxidation. Valid for both the hydrogen experiments see Section 3.3 and methane experiments 3.4. The values are at $T =$ 630K averaged over 90 discharges in joule per mole per pulse.

C_d	C_g	R_c	$\int i_c V_g dt$
4.05pF	0.57pF	1mΩ	2.60J/mol
8.10pF	0.57pF	1mΩ	5.24J/mol
4.05pF	1.14pF	1mΩ	2.55J/mol
8.10pF	1.14pF	1mΩ	5.22J/mol
4.05pF	0.57pF	50Ω	2.60J/mol
8.10pF	0.57pF	50Ω	5.22J/mol
4.05pF	1.14pF	50Ω	2.55J/mol
8.10pF	1.14pF	50Ω	5.19J/mol

From the table, it can be concluded that neither C_g nor R_c has a significant impact on the discharge energy, while, in these conditions, the coupled energy scales linearly with the dielectric constant. Therefore, it is likely that the estimate of the dielectric constant (C_d) is higher in Tsolas et al. [64] than in this work.

3.3. Results for hydrogen experiments

In Fig. 5 model results with the three different mechanisms are compared against the experimental results from Tsolas et al. [19]. At the lowest temperature, the consumption of hydrogen and oxygen is negligible in both experiments and measurements. With increasing temperature, both experiments and measurements show an increasing oxidation degree with a similar trend. Above $T =$ 850K all results show complete oxidation of the available hydrogen. While all three mechanisms qualitatively show similar trends, the quantitative behavior is slightly different. GRI-Mech 3.0 (dash-dot curves) shows the poorest match with the experimental results. The results computed using HP-mech (solid curves) show a better agreement with the measurements, but still show a significant difference in the range from 650 to 850K. Finally, the use of AramcoMech 2.0 (dashed curves) yields an excellent agreement with the experimental measurements of O_2 and H_2 concentration.

The uncertainty due to model parameters is also included via the dotted line. For these results, C_d has been doubled, which has the biggest impact on the coupled energy and thereby oxidation, see Table 1. This modification has only been included with AramcoMech 2.0 as the other mechanisms respond similarly. Based on the uncertainty due to the coupled energy, it can be safely concluded that all mechanisms are within the modeling uncertainty of these measurements.

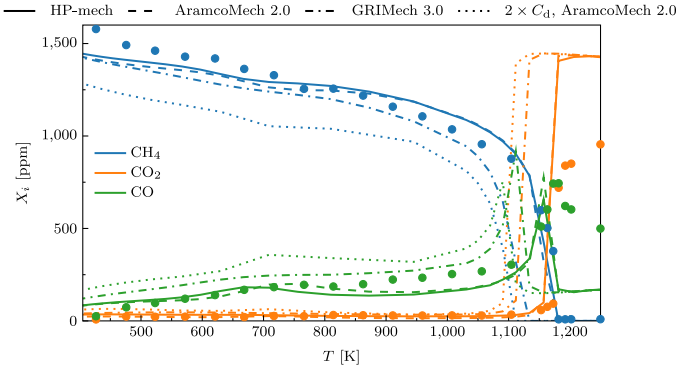

Fig. 6. Mole fractions of CH_4, CO_2 and CO as a function of reactor temperature, initial molar fractions are: $X_{Ar} = 0.9954$, $X_{O_2} = 3000$ppm and $X_{CH_4} = 1600$ppm. The solid lines are results obtained with HP-mech, dashed with AramcoMech 2.0, dash-dot with GRI-Mech 3.0, symbols are (measurements) from [42] and dotted AramcoMech 2.0 with twice the default C_d value.

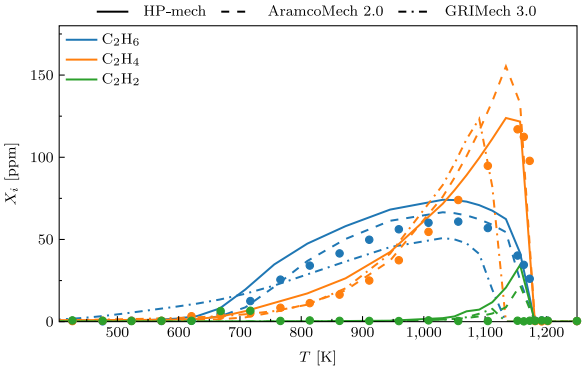

Fig. 7. Mole fractions of C_2H_6, C_2H_4 and C_2H_2 as a function of reactor temperature, initial molar fractions are: $X_{Ar} = 0.9954$, $X_{O_2} = 3000$ppm and $X_{CH_4} = 1600$ppm. The solid lines are results obtained with HP-mech, dashed with AramcoMech 2.0 and dash-dot with GRI-Mech 3.0, measurements are from [42].

3.4. Results for methane experiments

For methane, the available experimental data is more extensive. Major species (CO, CO_2 and CH_4) are depicted in Fig. 6, and minor species (C_2H_6, C_2H_4 and C_2H_2) in Fig. 7. Again, qualitatively all three mechanisms show a very similar trend to the experimental results from Tsolas et al. [18]. From the major species graph, we see that the CH_4 concentration decreases almost linearly from 400K to 1000K. At the same time, the CO_2 concentra-

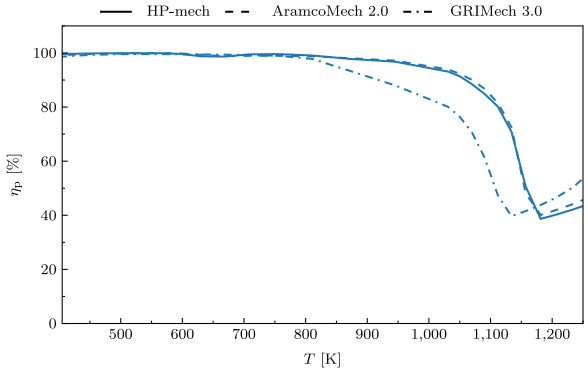

Fig. 8. The fraction of CH_4 that is consumed inside the plasma zone compared to the reactor outlet, initial molar fractions are: $X_{Ar} = 0.9954$, $X_{O_2} = 3000$ppm and $X_{CH_4} = 1600$ppm. The solid line is the result obtained with HP-mech, dashed with AramcoMech 2.0 and dash-dot with GRI-Mech 3.0.

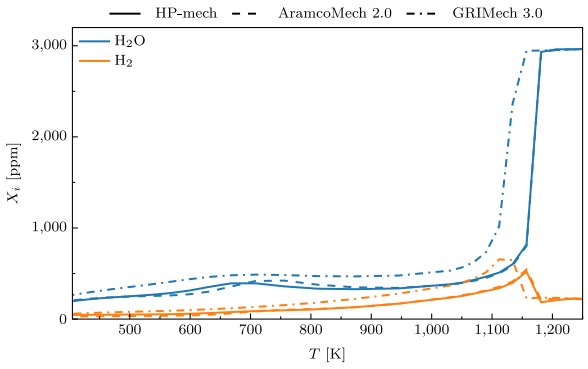

Fig. 9. Production of H_2O and H_2 as a function of reactor temperature, initial molar fractions are: $X_{Ar} = 0.9954$, $X_{O_2} = 3000$ppm and $X_{CH_4} = 1600$ppm. The solid lines are results obtained with HP-mech, dashed with AramcoMech 2.0 and dash-dot with GRI-Mech 3.0.

tion remains constant and nearly zero until 1100K. Above this temperature, the mixture ignites within the reactor (residence time) and is fully converted to products. The CO concentration initially increases linearly ($400 < T < 700$K) and then remains nearly constant until 1100K. When comparing the CO and CH_4 concentrations it is clear that the increase in CO can not account for the decrease in CH_4. This indicates that products other than CO are formed between 400 and 1100K.

When comparing the numerical results with the experimental results the GRI-Mech 3.0 (dash-dot) stands out: Ignition (see Fig. 6) occurs at a significantly lower temperature than for the experimental results and the other two mechanisms. However, the general trend is very similar, i.e., a downward slope in CH_4 concentration at a temperature below approximately 1000K, an increase in slope magnitude (for $T \geq 1000$K) and then ignition and full conversion. Both HP-mech and AramcoMech 2.0 show a bit more detail than GRI-Mech 3.0, e.g., a small bump near 700K, especially visible in the CO mole fraction. This can be explained by the limited low-temperature chemistry that is present in GRI-Mech 3.0. However, it is worth noting that this bump is not present in the measurements. For the major species, HP-mech and AramcoMech 2.0 give nearly identical results close to the experimental values. Moreover, they both capture the rapid transition around 1150K accurately. None of the mechanisms predicts the relatively large concentration of CO remaining above the ignition threshold. However, conditions above the ignition threshold are not the main focus of this article and thus not considered in our further analysis.

For the methane results (just as for hydrogen), the value of C_d is also doubled and simulations with AramcoMech 2.0 are included as the dotted line. Similar observations to the hydrogen case can be made, due to the increased C_d value the coupled energy is larger (see Table 1) as a result the oxidation increases. In the case of methane, a clear ignition threshold is visible, which is shifted to a lower temperature due to the increased coupled energy. Based on the uncertainty of the coupled energy (the default C_d is a lower bound), it can be concluded that GRI-Mech 3.0 is too reactive in these experiments. When accounting for the uncertainty due to the coupled energy, both the results from HP-mech and AramcoMech 2.0 can reproduce the experiments.

In Fig. 8 the converted fraction of CH_4 at the end of the plasma section is compared to that at the reactor outlet, i.e.,

$$\eta_p = \frac{X_{CH_4,0} - X_{CH_4,L_p}}{X_{CH_4,0} - X_{CH_4,L}}. \tag{14}$$

A value of 100% indicates that all CH_4 converted is consumed within the plasma section of the reactor. For all mechanisms, below 800K all CH_4 is converted within the plasma section of the reactor. This implies that the oxidation of methane, at these temperatures, does not occur without the aid of plasma. The minimum in these curves is the point at which ignition occurs within the flow reactor, i.e., the plasma generates precisely enough radicals for the ignition delay to occur within the residence time. Above this point, the plasma dissociates more methane than required for ignition to occur within the reactor. Within these simulations, ignition of methane does not occur within the plasma section of the reactor, otherwise, the fraction would return to 100%.

The main differences in measured and predicted species concentrations are visible for C_2H_2, see Fig. 7. All three mechanisms predict a very small amount of C_2H_2 near the ignition threshold, but this has not been observed experimentally. None of the mechanisms predicts the small amount of C_2H_2 produced between 650 and 750K in the experiments. A significant amount of C_2H_4 is predicted by all three mechanisms, which drops to zero at the ignition threshold. All three mechanisms predict a very similar trend: an exponential increase in the concentration starting at 600K. The magnitude of the peak at 1150K is captured most accurately by HP-mech, while AramcoMech 2.0 over-predicts the peak concentration. While GRI-Mech 3.0 captures the magnitude of the peak in C_2H_4 accurately, it does - due to the lower ignition temperature - predict it at a lower temperature. Overall, the trend for all mechanisms is very similar and the onset of C_2H_4 production is predicted accurately by all three mechanisms. Finally, the production of C_2H_6 starts at the lowest temperature (in the numerical models), the trend is well represented by both AramcoMech 2.0 and HP-mech, while the onset of C_2H_6 production is significantly underpredicted by GRI-Mech 3.0. The magnitude of C_2H_6 production is most accurately captured by AramcoMech 2.0.

In Fig. 9, the simulated production of H_2O and H_2 is illustrated. The predicted trend of H_2O production is very similar to the CO production in Fig. 6. The main difference is that the CO concentration returns to a low value above the ignition temperature, while H_2O increases. When comparing the CO and H_2O concentration from 405 to 1000K, it can be noted that the H_2O concentration is approximately twice that of CO. This implies either that a small amount of atomic H is released in the partial oxidation of CH_4 or that H_2 is formed. This is confirmed by the profile of the production of H_2: It increases with an increase in reactor temperature and decreases above ignition.

Finally, in Fig. 10 the simulated production of methanol (CH_3OH) and formaldehyde (CH_2O) is shown. Unfortunately, no measurements for these species are available, but we have included the numerical results anyway as they are stable intermediates. Moreover, the most significant differences between the mechanisms are present in these results. The results obtained

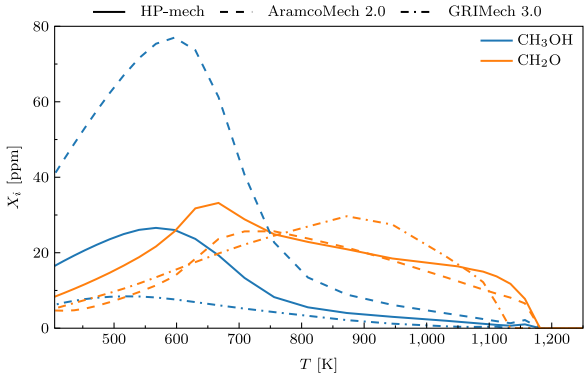

Fig. 10. Mole fractions of CH_3OH and CH_2O against reactor temperature, initial molar fractions are: $X_{Ar} = 0.9954$, $X_{O_2} = 3000$ppm and $X_{CH_4} = 1600$ppm. The solid lines are results obtained with HP-mech, dashed with AramcoMech 2.0 and dash-dot with GRI-Mech 3.0.

by AramcoMech 2.0 show a significant amount of CH_3OH below 700K, while GRI-Mech 3.0 shows nearly no CH_3OH. Above 800K the three mechanisms, show a qualitatively similar trend in the CH_3OH production; a nearly linear decrease until the ignition temperature. The difference in the production of CH_2O is much smaller. The shape of the CH_2O curve predicted by using AramcoMech 2.0 and HP-mech are rather similar. However, the peak present in the HP-mech results, around 650K, is not present in the AramcoMech 2.0 results. Above 700K both AramcoMech 2.0 and HP-mech predict a linear decrease in the CH_2O production with a sharp drop at the ignition threshold. Again, GRI-Mech 3.0 predictions are rather different from those of the other two mechanisms, which show a smooth hill with a peak at 900K.

4. Pathways in low-temperature hydrogen oxidation

To analyze differences between plasma-assisted H_2 and CH_4 oxidation, pathway analysis is performed. The rates of reaction progress are integrated over the residence time inside the plasma section of the reactor to obtain the net conversion by each reaction. We have opted to only integrate the chemical rates of progress over the plasma section as this will provide the most insight into the combustion activation via the plasma. When the rates of progress are integrated over the entire domain chemical runaway via conventional high-temperature pathways will dominate the chemistry above 1150K (or 1100K in GRI-Mech 3.0).

This integral analysis shows that the rate of thermal decomposition of H_2 and O_2 by

$$H_2 + M \leftrightarrow 2H + M \tag{R.2}$$

and

$$O_2 + M \leftrightarrow 2O + M \tag{R.3}$$

is very low. The initial H radicals are provided via the reaction of H_2 with excited argon,

$$H_2 + Ar^* \leftrightarrow 2H + Ar, \tag{R.4}$$

which deactivates an electronically excited Ar atom and produces two hydrogen radicals (dissociative quenching). At the same time, initial O radicals are produced by the plasma through the reaction:

$$O_2 + Ar^* \leftrightarrow 2O + Ar. \tag{R.5}$$

Over the entire temperature range, the rate of progress of reactions R.4 and R.5 is six orders of magnitude higher than the conventional dissociation reactions (R.2 and R.3). Reactions R.4 and R.5 are the only reactions competing for the available Ar^* as physical quenching, via

$$Ar^* + Ar \leftrightarrow 2Ar \tag{R.6}$$

or

$$Ar^* + 2Ar \leftrightarrow 3Ar \tag{R.7}$$

is significantly slower. The excited argon required in reactions R.4 and R.5 is produced via the plasma reaction:

$$Ar + e \rightarrow Ar^* + e. \tag{R.8}$$

The reactions identified above are the only reactions involving electronically excited states that contribute at least 5% to the oxidation of hydrogen. The reactions involving electronically excited O or O_2 are only a minor contribution to the oxidation. This observation has also been made by Togai et al. [49] in their sensitivity analysis of these experiments. The observation is due to the low concentration of oxygen ($X_{O_2} = 3000$ppm), making it far less likely that electronically excited O_2 or O is produced by electron impact. For example, in Snoeckx et al. [30] the O_2 concentration is much higher, and O(1D) is found to be important to the oxidation of hydrogen.

4.1. Low-temperature radical cycle

The hydrogen radicals produced in R.4 are converted into HO_2 via

$$H + O_2(+M) \leftrightarrow HO_2(+M). \tag{R.9}$$

The oxygen radicals produced by the plasma (R.5) attack the relatively stable HO_2 and form OH via

$$HO_2 + O \leftrightarrow O_2 + OH. \tag{R.10}$$

When the temperature is less than 450K (depending on the mechanism), most of the OH reacts with the available O radicals and forms:

$$OH + O \leftrightarrow O_2 + H. \tag{R.11}$$

This creates a cyclic process of reactions R.9, R.10 and R.11, where, with every roundtrip, two O atoms are recombined. Via this cycle, the O atoms produced via Ar^* quenching (R.5) are removed from the radical pool, without progressing the H oxidation. Two reactions are active, which do progress the oxidation,

$$HO_2 + OH \leftrightarrow O_2 + H_2O, \tag{R.12}$$

which removes two O atoms from the radical pool but also produces H_2O, and

$$OH + H_2 \leftrightarrow H_2O + H, \tag{R.13}$$

which produces H_2O and a H radical. Reaction R.12 and R.13 do compete with R.10 and R.11 for the available HO_2 and OH respectively. However, R.10 and R.11 are significantly faster such that the majority of the H atoms are cycled in the reaction chain of R.9, R.10 and R.11.

4.2. Mid-temperature radical cycle

Under the conditions of these experiments, R.13 becomes dominant over R.11 above 450K. A new cycle of reactions R.9, R.10 and R.13 forms, which consumes one oxygen radical per roundtrip and produces one H_2O. Therefore, this cycle is significantly more efficient at oxidizing hydrogen than the earlier mentioned cycle (see the low-temperature and mid-temperature illustration in Fig 11). This can be used to explain the low-oxidation degree at 400K and the increase of the oxidation degree beyond that, as it is observed in Fig. 5.

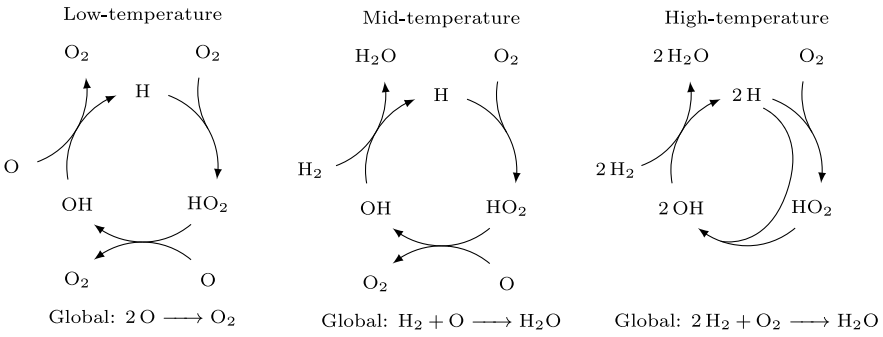

Fig. 11. Simplified low-temperature to high-temperature radical cycle for the oxidation of hydrogen. The low-temperature cycle does not progress the oxidation, while the mid-temperature and high-temperature cycles do progress the oxidation. In the low-temperature and mid-temperature cycle, the size of the radical pool slowly decreases, while in the high-temperature cycle the radical pool remains constant.

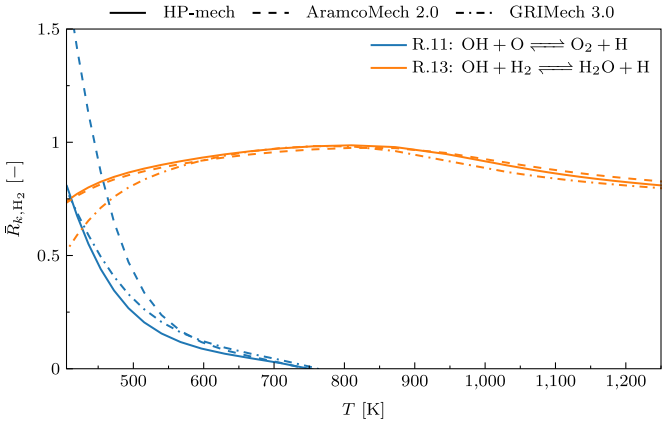

Fig. 12. Normalized mean reaction rate for reaction R.11 and R.13 for the three different mechanisms, initial molar fractions are: $X_{Ar} = 0.995$, $X_{O_2} = 3000$ppm and $X_{H_2} = 2000$ppm. The solid lines are results obtained with HP-mech, dashed with AramcoMech 2.0 and dash-dot with GRI-Mech 3.0. Below 450K R.11 is the preferred pathway while for increased temperature R.13 is preferred. Above 750K reaction R.11 is run in reverse.

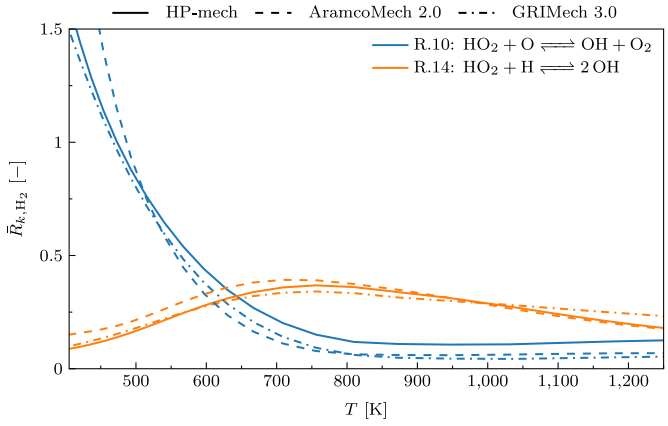

Fig. 13. Normalized mean reaction rate for reaction R.10 and R.14 for the three different mechanisms, initial molar fractions are: $X_{Ar} = 0.995$, $X_{O_2} = 3000$ppm and $X_{H_2} = 2000$ppm. The solid lines are results obtained with HP-mech, dashed with AramcoMech 2.0 and dash-dot with GRI-Mech 3.0. At low-temperature R.10 is the preferred pathway while for increased temperature R.14 is preferred.

To illustrate this change, the integrated rate of progress of each reaction is normalized by the total H_2 consumption, i.e.:

$$\bar{R}_{k,H_2} = \frac{\int_0^{\tau_p} R_k dt}{\int_0^{\tau_p} \omega_{H_2} dt}, \tag{15}$$

where k is the reaction index and subscript H_2 is used to indicate that this has been normalized with respect to H_2 consumption. This makes $\bar{R}_{k,H_2}$ the mean normalized reaction rate of reaction k, which makes it an indicator of the importance of a certain reaction on the overall conversion. Negative values are possible, which indicates that the reaction ran in reverse. Values above 1.0 (or below -1.0) are also possible when the reaction only involves a single H atom. For reactions R.11 and R.13, these normalized mean reaction rates are depicted in Fig. 12 as a function of reactor temperature. From this graph, it can be seen that R.11 is the preferred pathway below 450K, but when the temperature is increased, R.13 quickly becomes dominant. Over the entire range of 600 to 1260K almost all H_2 is converted into H_2O using this reaction ($\bar{R}_{R.13,H_2} \approx 1$). When comparing the three different mechanisms, AramcoMech 2.0 stands out because the temperature at which R.13 becomes dominant over R.11 occurs at a higher temperature of 450K instead of 400K. This explains why the H_2 conversion below 550K using AramcoMech 2.0 is slightly less than that of HP-mech and GRI-Mech 3.0 (see Fig. 5). However, above 600K, the normalized rates of R.13 in the three mechanisms converge and the mechanisms predict very similar results.

The series of reactions R.9, R.10 and R.13, only require oxygen radicals to run (see mid-temperature illustration Fig. 11). This implies that reaction R.5 has a positive effect on oxidation, while reaction R.4 only quenches Ar^* without significantly progressing the oxidation. Of course, reaction R.4 is still required to provide an initial pool of H radicals, but beyond that, it is in direct competition with reaction R.5 and inhibits oxidation. Note, the illustrated cycle is not chain branching and linearly depends on the number of Ar^* produced by the plasma (see R.8). The degree of oxidation, below the explosion limit, is expected to be linearly dependent on the coupled energy.

4.3. High-temperature radical cycle

When the temperature is increased further, the reaction of HO_2 with H,

$$HO_2 + H \leftrightarrow 2OH, \tag{R.14}$$

becomes competitive with reaction R.10. The cyclic process then evolves into the high-temperature graph of Fig. 11. This new cycle is distinctly different. While the size of the radical pool (sum of H, OH and HO_2 radicals) is slowly decreasing for the low and mid-temperature two cycles, it remains constant for the high-temperature one. This is because R.14 produces two OH molecules and thus R.13 is run twice, which leaves one extra H to supply R.14. For both these reactions the normalized mean reaction rate is computed and shown in Fig. 13. Below 600K, R.10 is the dominant pathway and above 600K, R.14 is preferred.

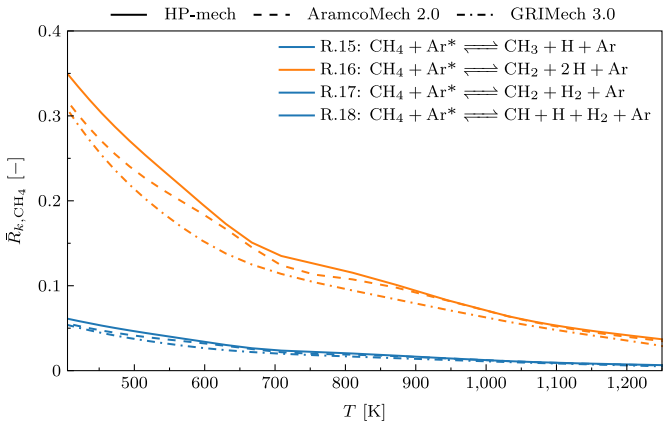

Fig. 14. Normalized mean reaction rate for reaction R.15, R.16, R.17 and R.18 for the three different mechanisms, initial molar fractions are: $X_{Ar} = 0.9954$, $X_{O_2} = 3000$ppm and $X_{CH_4} = 1600$ppm. The rates of reactions R.15, R.17 and R.18 are identical, which is why these are displayed with a single color. The solid lines are results obtained with HP-mech, dashed with AramcoMech 2.0 and dash-dot with GRI-Mech 3.0.

The change in the different chemistry modes, as illustrated in Fig. 11, explains why the oxidation accelerates with temperature (see Fig. 5). From low to high temperature, the chemistry becomes more efficient at oxidizing the available H_2. Moreover, as the dominant pathways change smoothly, see Fig. 12 and Fig. 13, and the mid and high-temperature modes remain mixed, no clear ignition threshold is observed. Finally, these three modes can also be used to explain the sustained reactivity observed in recent flow reactor experiments by Jans et al. [21]. In the measurements of 300 and 400K, only the low-temperature mode is active. As a result, the radical chemistry quickly recombines the plasma-generated O radicals back into O_2 and the HO_2 concentration will decrease directly after the plasma is stopped. When the temperature is increased, first the mid-temperature mode is activated - for which it is still expected that the HO_2 concentration decays after the removal of the plasma (as it consumes one O radical and thus depletes the radical pool) - and finally, the high-temperature mode is activated - for which it is expected that the HO_2 concentration will remain nearly constant for some time after plasma activation (as the cycle itself does not consume radicals). The sustained HO_2 concentration after plasma activation is an indication of self-sustained reactivity. This leads to the conclusion that in these conditions the plasma can be used to accelerate the initiation reactions, after which chain branching takes over and H_2 is quickly oxidized.

5. Pathways in low-temperature methane oxidation

The oxidation of methane is significantly more complicated than that of hydrogen. Our analysis follows the carbon atoms in CH_4. The plasma dissociates CH_4 via

$$CH_4 + Ar^* \leftrightarrow CH_3 + H + Ar, \quad \text{(R.15)}$$

$$CH_4 + Ar^* \leftrightarrow CH_2 + 2H + Ar, \quad \text{(R.16)}$$

$$CH_4 + Ar^* \leftrightarrow CH_2 + H_2 + Ar \quad \text{(R.17)}$$

and

$$CH_4 + Ar^* \leftrightarrow CH + H + H_2 + Ar, \quad \text{(R.18)}$$

where R.16 is more than five times faster than R.15, R.18 and R.17 (which have equal rates). In Fig. 14, the normalized mean reaction rates for R.16 and R.15 are shown. The normalized mean reaction rates for R.18 and R.17 are equal to that of R.15 since the rate constants are equal, which is why they are not shown in Fig. 14. Note, differences between the mechanisms in these normalized mean reaction rates are not due to different rate constants but are due to differences in the non-plasma pathways. The consumption of CH_4 occurs for nearly 50% via quenching of Ar^* ($\sum_{k=15}^{18} \bar{R}_{k,CH_4} \approx 0.45$) at $T = 400$K and this fraction reduces with increasing temperature. Even though a small fraction (less than 10% for $T > 900$K) of methane is converted by plasma reactions, the impact on the overall oxidation rate is not small (without plasma the mixture does not oxidize [18]). These plasma reactions are very fast and replace slow initiation reactions, like reactions R.3 and

$$CH_4(+M) \leftrightarrow CH_3 + H(+M), \quad \text{(R.19)}$$

meaning that these plasma reactions accelerate the overall oxidation by the generation of initial radicals. Just as for hydrogen, our analysis did not identify reactions involving O_2 or O electronically excited states to significantly contribute to the oxidation. Again, this is likely due to the low concentration of O_2, which makes the production of excited O_2 and O less likely.

5.1. The CH_2 pathway

The CH_2 produced by R.16 reacts with the abundantly available O_2 via the essentially barrierless reaction (with activation temperature $T_a = 754$K):

$$CH_2 + O_2 \leftrightarrow HCO + OH. \quad \text{(R.20)}$$

Again, a practically barrierless reaction ($T_a = 206$K) follows, which produces CO:

$$HCO + O_2 \leftrightarrow CO + HO_2. \quad \text{(R.21)}$$

In both HP-mech and GRI-Mech 3.0, an alternative path is present to convert CH_2 into CO, skipping the formation of HCO:

$$CH_2 + O_2 \rightarrow CO + H + OH. \quad \text{(R.22)}$$

This path, only available in HP-mech and GRI-Mech 3.0, produces an H radical instead of the HO_2 radical. However, just as in the hydrogen case, reaction R.9 quickly converts H radicals into HO_2. This implies that the net effect on mixture the composition of R.22 is similar to the reaction chain R.22 and R.21.

The above series of reactions (R.22 and R.21 or R.22) requires the formation of Ar^* by the plasma, but after that, it only involves reactions with O_2 that have a low activation energy. Thus, this short chain of reactions explains why a small fraction of methane is converted to CO (see Fig. 6), even at the lowest reactor temperature. It should also be noted that this plasma-activated pathway produces OH and HO_2 radicals, which, as we will later see, allow oxidation via a more conventional CH_4 oxidation pathway. CO is not a radical and requires high temperatures and preferably the presence of OH, to oxidize into CO_2. As a result, the plasma is not able to completely oxidize CH_4 into CO_2 until the ignition threshold (Fig 6).

5.2. Formation of CH_3OH

When considering AramcoMech 2.0, the above chain produces two H radicals, one OH and one HO_2 radical. These radicals are utilized in an alternative pathway, which results in an enhancement over just the consumption of CH_4 by reactions R.15 and R.16. Most of the OH produced in Reaction R.20 (or R.22 in HP-mech and GRI-Mech 3.0) activates this pathway via

$$CH_4 + OH \leftrightarrow CH_3 + H_2O. \quad \text{(R.23)}$$

When the temperature is increased, H (produced by R.16 and R.15) or O radicals are also used to dissociate methane into methyl (CH_3) via the reactions

$$CH_4 + H \leftrightarrow CH_3 + H_2 \quad \text{(R.24)}$$

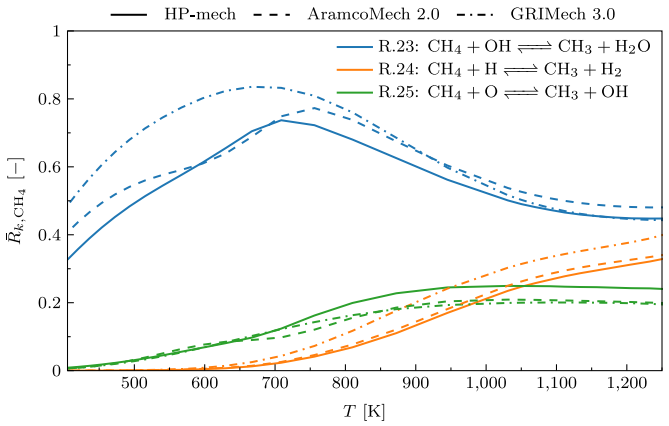

Fig. 15. Normalized mean reaction rate for reaction R.24, R.25 and R.23 for the three different mechanisms, initial molar fractions are: $X_{Ar} = 0.9954$, $X_{O_2} =$ 3000ppm and $X_{CH_4} = 1600$ppm. The solid lines are results obtained with HP-mech, dashed with AramcoMech 2.0 and dash-dot with GRI-Mech 3.0.

and

$$CH_4 + O \leftrightarrow CH_3 + OH. \quad \text{(R.25)}$$

The normalized mean reaction rate for these three reactions is depicted in Fig. 15. In all three mechanisms, we see a similar trend. Below 600K, predominantly the reaction with OH is active. The remainder of the CH_4 is consumed by Ar* quenching reactions R.15 till R.18 (see also Fig. 14). As the temperature is increased, the dissociation of methane via radical attack becomes more important. This is both because the reactions R.24, R.25 and R.23 become faster when the temperature is increased - as they have a relatively large activation energy - as well as an increase in the radical concentration. Reaction R.23 via OH is found to be practically the only pathway for methane dissociation below 800K. Above 900K, all three reactions significantly contribute to the dissociation of methane. In Fig. 6, it can be seen that this corresponds to the temperature at which the consumption of CH_4 starts accelerating. The differences between the three mechanisms are significant:

1. In GRI-Mech 3.0 (dash-dot) the importance of R.23 ($T < 900$K) and R.24 ($T > 700$K) is 0.1 0.2 higher compared to AramcoMech 2.0 and HP-mech.
2. AramcoMech 2.0 (dashed) shows a dip in the upwards trend of the normalized mean reaction rate of R.23 between 450 and 750K, which is not present in GRI-Mech 3.0 and HP-mech.
3. Even above the traditional ignition threshold ($T > 1200$K) differences remain. Each mechanism shows a slight preference for a different reaction.

When the concentration of O radicals is insufficient, the oxidation progresses via methoxide CH_3O instead of formaldehyde CH_2O. This is generally the case when the temperature is low ($T <$ 950K). Two possible pathways are identified: In the first, when the temperature is below 750K, the CH_3 radical predominantly reacts with the available oxygen,

$$CH_3 + O_2(+M) \leftrightarrow CH_3OO(+M). \quad \text{(R.26)}$$

The CH_3OO then reacts with the H produced by reactions R.15 and R.16 in reaction,

$$CH_3OO + H \leftrightarrow CH_3O + OH, \quad \text{(R.27)}$$

or with O in reaction

$$CH_3OO + O \leftrightarrow CH_3O + O_2. \quad \text{(R.28)}$$

In the second, between 700 and 950K, a fraction of the CH_3 directly forms CH_3O using the HO_2 produced in reaction R.21:

$$CH_3 + HO_2 \leftrightarrow CH_3O + OH. \quad \text{(R.29)}$$

Below 700K the oxidation of CH_3O progresses through methanol (CH_3OH), either via reaction

$$CH_3O + HO_2 \leftrightarrow CH_3OH + O_2 \quad \text{(R.30)}$$

or via

$$CH_3OO + OH \leftrightarrow CH_3OH + O_2. \quad \text{(R.31)}$$

It is also possible to form CH_3OH directly out of CH_3 via reaction

$$CH_3 + OH(+M) \leftrightarrow CH_3OH(+M), \quad \text{(R.32)}$$

which we identify as a minor pathway. Note that the series of reactions that convert CH_4 into CH_3OH has a chain-terminating nature: Reactions R.25, R.27, and R.29 do produce OH radicals, but these are quickly consumed by the abundantly available CH_4 and converted into H_2O (R.23). Moreover, reactions R.31 and R.32 consume OH, while reaction R.30 requires HO_2. In other words, the production of CH_3OH from CH_4 removes OH from the radical pool. The removal of radicals by this initiation step of oxidation (R.23) also explains that a significant amount of CH_4 can be consumed without ignition (Fig. 6). From the above analysis it is revealed that the size of the radical pool is effectively controlled by the amount of CH_4 present, i.e., the explosive growth of the radical pool is not possible. As H atoms produced by the plasma - reactions R.15, R.16, R.17 and R.18 - are quickly removed from the radical pool (H, OH and HO_2), further oxidation beyond CH_3OH is inhibited by the presence of CH_4. As a result, a significant amount of CH_3OH is produced by the plasma below 700K (see Fig. 10) and the CO concentration remains rather constant up to this temperature (see Fig. 6).

The reaction paths predicted by the three different mechanisms show a rather significant difference in this early stage of oxidation. In GRI-Mech 3.0, the CH_3OO species is not present, such that the path of reaction R.26 followed by R.27 is not possible. Instead, in GRI-Mech 3.0, reaction R.29 is the only dominant path to produce CH_3O. In both GRI-Mech 3.0 and HP-mech reaction R.30 is not present, which reduces the production of methanol in GRI-Mech 3.0 to practically zero, and in HP-mech it more than halves it compared to AramcoMech 2.0 (see Fig. 10). The absence of reaction R.30 in both GRI-Mech 3.0 and HP-mech is noteworthy, as it is identified by both Metcalfe et al. [34] and Li et al. [65] as the third most sensitive reaction in the oxidation of CH_3OH. At the same time, it should be noted that reaction R.31 is implemented in the reverse direction in AramcoMech 2.0, as that is the direction in which it progresses during the oxidation of CH_3OH. In a numerical study by [66], the rate constant in the direction defined in reaction R.31, was found to be barrierless and independent of temperature, which is not the case in AramcoMech 2.0.

5.3. The CH_2O pathway

Just as in the conventional oxidation of CH_4, formaldehyde CH_2O is an important intermediate in plasma-assisted oxidation below 950K. Three dominant pathways are identified that progress the oxidation of CH_4 towards CH_2O. The first, below 700K the main oxidation progresses via methanol (especially in AramcoMech 2.0):

$$CH_3OH + OH \leftrightarrow CH_2OH + H_2O, \quad \text{(R.33)}$$

followed by,

$$CH_2OH + O_2 \leftrightarrow CH_2O + HO_2. \quad \text{(R.34)}$$

The second, at elevated temperatures ($700 < T < 950$K) the oxidation directly progresses via the conversion of methoxide CH_3O to CH_2O following the reactions:

$$CH_3O(+M) \leftrightarrow CH_2O + H(+M) \quad \text{(R.35)}$$

and

$$CH_3O + O_2 \leftrightarrow CH_2O + HO_2. \quad \text{(R.36)}$$

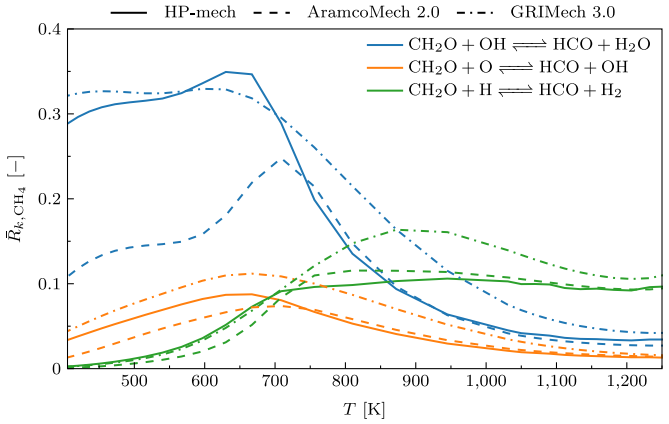

Fig. 16. Normalized mean reaction rate for reaction R.42, R.41 and R.40 for the three different mechanisms, initial molar fractions are: $X_{Ar} = 0.9954$, $X_{O_2} =$ 3000ppm and $X_{CH_4} =$ 1600ppm. The solid lines are results obtained with HP-mech, dashed with AramcoMech 2.0 and dash-dot with GRI-Mech 3.0.

In both GRI-Mech 3.0 and HP-mech an alternative and faster reaction is

$$CH_3O + O \leftrightarrow CH_2O + OH, \tag{R.37}$$

which is not present in AramcoMech 2.0. The third is the formation of CH_2O directly from CH_3:

$$CH_3 + O \leftrightarrow CH_2O + H, \tag{R.38}$$

which only occurs if the O radical pool is sufficiently large. As an alternative to R.38, the reaction with O_2 is also possible,

$$CH_3 + O_2 \leftrightarrow CH_2O + OH, \tag{R.39}$$

which has a high activation energy. Generally, R.38 and R.39 are only relevant at higher temperatures (R.39) or when a significant portion of the CH_4 has been consumed, such that the concentration of atomic O can increase as R.38 competes with R.25.

The oxidation from CH_2O to CO is similar for the whole temperature range. Three different reactions can form formyl (HCO) from CH_2O:

$$CH_2O + OH \leftrightarrow HCO + H_2O, \tag{R.40}$$

$$CH_2O + O \leftrightarrow HCO + OH \tag{R.41}$$

and

$$CH_2O + H \leftrightarrow HCO + H_2. \tag{R.42}$$

HCO is then converted to CO by reaction R.21. In Fig. 16, the branching between these three reactions is shown: Over the entire temperature range, R.41 has only a small contribution to the overall oxidation of CH_2O. Below 700K, the reaction utilizing OH (R.40) is the main pathway for CH_2O consumption, while above 1000K, R.42 is preferred. The significant difference below 700K between AramcoMech 2.0 (dashed) and the other two is due to the differences in methanol formation discussed earlier. As a result of this difference, more CH_3OH is formed when AramcoMech 2.0 is utilized and thus less CH_2O is produced, see Fig. 10. This implies that less CH_2O is available for reactions R.42, R.41 and R.40. Besides the large difference below 700K, the differences between AramcoMech 2.0 and HP-mech are remarkably small; above 700K the relative differences are less than 30%, especially when you consider that this is one of the later steps in the oxidation of CH_4. In other words, many earlier oxidation steps have already introduced their differences.

5.4. The C_2H_6 pathway

The series of reactions involved in the C_2H_6 pathway can be used to explain the results of 7. Starting at 800K chemical pathways via alkane growth are important to the overall oxidation. The first step is via

$$CH_3 + CH_3(+M) \leftrightarrow C_2H_6(+M), \tag{R.43}$$

which is competitive with the oxidation reactions of methyl (R.26, R.29 and R.38). This reaction is followed by

$$C_2H_6 + OH \leftrightarrow C_2H_5 + H_2O, \tag{R.44}$$

$$C_2H_6 + O \leftrightarrow C_2H_5 + OH \tag{R.45}$$

and

$$C_2H_6 + H \leftrightarrow C_2H_5 + H_2. \tag{R.46}$$

The produced ethyl radical (C_2H_5) is unstable and quickly reacts via

$$C_2H_5(+M) \leftrightarrow C_2H_4 + H(+M). \tag{R.47}$$

The oxidation then continues either via

$$C_2H_4 + O \leftrightarrow HCO + CH_3, \tag{R.48}$$

followed by the HCO chain (R.21), or via

$$C_2H_4 + H \leftrightarrow C_2H_3 + H_2 \tag{R.49}$$

and

$$C_2H_4 + OH \leftrightarrow C_2H_3 + H_2O, \tag{R.50}$$

where, C_2H_3 is unstable and quickly forms acetylene C_2H_2,

$$C_2H_3(+M) \leftrightarrow C_2H_2 + H(+M). \tag{R.51}$$

From this pathway, we observe that the formation of C_2H_6 is required before C_2H_4 can be formed, which in turn is required for the formation of C_2H_2. Using this C_2H_x pathway, the presence of C_2H_2 between 600 and 800K and the lack of it between 1000 and 1200K in the experiments (Fig. 7) can not be explained. While not shown here, the predicted concentration of the intermediates in this chain (C_2H_5 and C_2H_3) is negligible at the outlet.

After the formation of C_2H_2, this oxidation chain is relatively straightforward. First, C_2H_2 is attacked by an O radical,

$$C_2H_2 + O \leftrightarrow HCCO + H, \tag{R.52}$$

followed by

$$HCCO + H \leftrightarrow CH_2(S) + CO, \tag{R.53}$$

where the produced singlet state of CH_2 quickly quenches to the ground state. After it has been quenched, the oxidation continues via R.20 and R.21 to CO.

5.5. Contribution of pathways

In the previous three sections, we have identified four different plasma oxidation pathways:

1. The plasma-induced CH_2 pathway; excited argon atoms dissociate CH_4 into CH_2, which quickly oxidizes into CO.
2. At the lowest temperatures the oxidation progresses via CH_3OH and then into CH_2O.
3. For intermediate temperature the oxidation skips CH_3OH and directly forms CH_2O either from CH_3 or CH_3O.
4. For the highest temperature the oxidation initially forms C_2H_6 which is then progressively broken down until CO is formed.

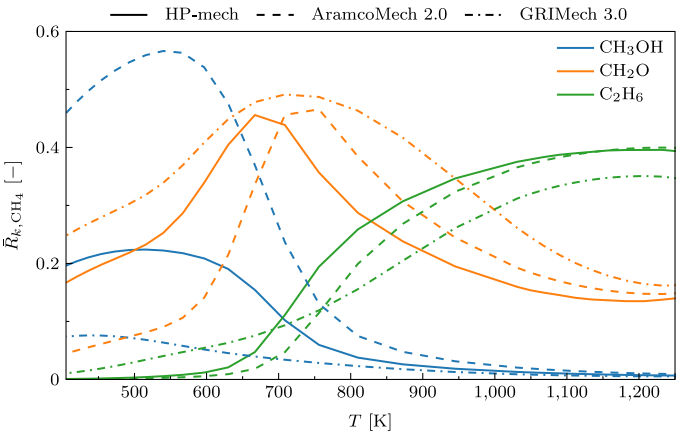

Fig. 17. Normalized mean reaction rate for reaction the main oxidation pathways of methane, initial molar fractions are: $X_{Ar} = 0.9954$, $X_{O_2} = 3000$ppm and $X_{CH_4} = 1600$ppm. The solid lines are results obtained with HP-mech, dashed with AramcoMech 2.0 and dash-dot with GRI-Mech 3.0.

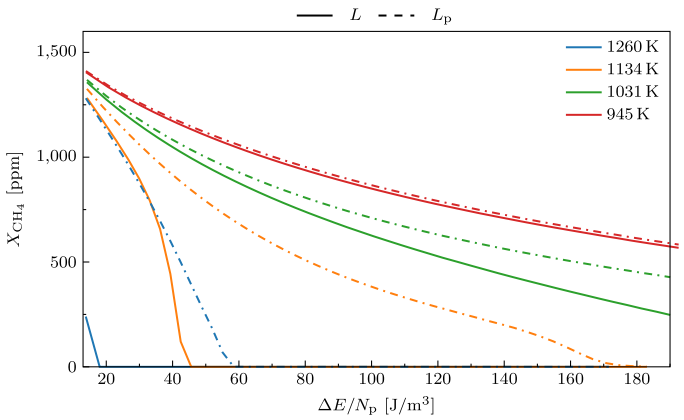

Fig. 18. Methane concentration after the plasma section (dashed) and at the exhaust (solid) for varying deposited energy, initial molar fractions are: $X_{Ar} = 0.9954$, $X_{O_2} = 3000$ppm and $X_{CH_4} = 1600$ppm. The deposited energy for these simulations in previous figures was: 30 (1260K), 33 (1134K), 35 (1031K) and 38J/m^3 (945K).

The normalized mean reaction rate of pathway 1 is shown in Fig. 14, which is easy to illustrate as it is only activated by R.16 and R.17. However, the normalized mean reaction rate of pathways 2 to 4 are more challenging to illustrate, as differences in the reaction mechanisms imply slight nuances in their activation. To still compare the contribution of the different pathways to the overall conversion for different reaction mechanisms, we have compared different reactions with a similar chemical effect. To obtain the normalized mean reaction rate of CH_3OH in AramcoMech 2.0, we have added the rates of reactions R.31, R.30 and R.32. As explained before, in HP-mech R.30 is not included and in GRI-Mech 3.0 R.30 and R.31 are not included. In the normalized mean reaction rate of CH_2O, we have excluded the CH_3OH pathway (R.33 followed by R.34) as that is considered to be part of the CH_3OH path. In all mechanisms the following reactions: are considered R.35, R.36, R.39 and R.38. The additional reaction (R.37) in HP-mech and GRI-Mech 3.0 is also included in their contribution. Finally, the normalized mean reaction rate of pathway 4 (C_2H_6) is activated only by R.43. These normalized mean reaction rates of the different pathways are depicted in Fig. 17. All three mechanisms show a similar qualitative trend: the CH_3OH pathway is only active below 700K, the CH_2O pathway is dominant between 600 and 900K and the C_2H_6 pathway is active above 700K. The large difference in CH_3OH and CH_2O pathways is due to the differences explained in Section 5.2. Above 800K, HP-mech and AramcoMech 2.0 show a very similar branching over the pathways. GRI-Mech 3.0 has (relative to HP-mech and AramcoMech 2.0) changes in a relatively wide temperature range from one pathway to the other.

5.6. The last step: CO to CO_2

The final step of oxidation is the conversion of CO to CO_2, which is rather slow. For it to occur at a decent rate the presence of OH is required in the reaction

$$CO + OH \leftrightarrow CO_2 + H. \quad \text{(R.54)}$$

As the concentration of OH is suppressed by the presence of CH_4 due to R.23, the CO to CO_2 reaction can only occur when most methane is removed. Moreover, above 650K the rate constant of R.23 is larger than R.54, which explains the lack of CO_2 below the ignition threshold, as it can only be formed when CH_4 is depleted.

5.7. Energy dependence of methane oxidation

The oxidation of methane is strongly inhibited by the presence of methane itself. If methane is present in a significant concentration and the temperature is below 900K, OH is quickly removed from the radical pool by CH_4. The produced CH_3 radical then converts into either CH_3OH ($T < 700$K) or CH_2O ($T < 1000$K). Neither the production of CH_3OH nor the production of CH_2O out of CH_3 releases sufficient radicals to compensate for the consumption of these radicals by CH_4 itself. This implies that it is challenging to ignite this diluted mixture of methane below 1000K.

The difficulty of igniting this mixture is illustrated in Fig. 18, where the deposited energy dependence of the CH_4 consumption is shown. These simulations have been conducted at four reactor temperatures. The dashed line is the CH_4 concentration directly after the plasma ($x = L_p$), while the solid line is at the exhaust ($x = L$). Only the results of AramcoMech 2.0 are shown, as the other two mechanisms lead to the same observations. The modification of the coupled energy is obtained by modifying the peak voltage from 5 to 50kV of the discharge, as $\Delta E/N_p \propto \max(V_s)$.

The concentration of CH_4 after L_p reduces nearly linearly with increasing deposited energy until it is completely consumed. Interestingly, no clear ignition threshold is present if all CH_4 is consumed within the plasma. At low reactor temperatures ($T \leq 1031$K) the CH_4 concentration also decreases linearly with increased deposited energy. When the reactor temperature is 1260K the mixture can ignite within L if the deposited energy is larger than 20J/m^3. For the reduced reactor temperature of 1134K, the mixture is not able to ignite for the default 10kV peak voltage or 33J/m^3 deposited energy, see also Fig. 6. If the deposited energy is increased the difference between the methane consumed within L_p and L increases. This indicates that the mixture exhibits reactivity without plasma present. When $\Delta E/N_p > 40$J/m^3 a mixture at 1134K can ignite within L. Just below the ignition threshold, the consumption of CH_4 shows a non-linear dependence on the deposited energy. We can also observe that at 1134K more than four times the energy is required to ignite the mixture within L_p, while the residence time is $L_p/L = 9$ times shorter.

When the reactor temperature is reduced even further to 1031 or 945K, the mixture is not able to ignite within the residence time of the reactor, even though more than five times the energy is deposited (the deposited energy in all previous graphs was 35 and 38J/m^3 for 1031 and 945K respectively). For reduced temperature, the reactivity of the mixture after the plasma section reduces strongly, which indicates that the plasma does not induce sustained reactivity. Moreover, the lack of an ignition threshold - even though more than 85% of methane is consumed for $T = 1031$K - suggests that plasmas can not significantly modify the minimum ignition temperature. This suggests that plasma is excellent at tem-

porarily increasing the reactivity and thereby reducing the ignition delay, but is unable to induce ignition when the mixture is not hot enough by itself.

6. Conclusion

In this work, we have investigated low-temperature plasma-assisted combustion using three different combustion mechanisms. The combined plasma-assisted combustion mechanisms are made available through the Supplementary Materials. The model and chemical mechanisms are validated against experimental data in a diluted flow reactor for both $H_2/O_2/Ar$ and $CH_4/O_2/Ar$ mixtures. Generally, a good qualitative agreement is observed for all mechanisms and both fuels. In the hydrogen simulations, excellent agreement is obtained with the AramcoMech 2.0 mechanism. However, due to the lack of deposited energy measurements in the experiments, large uncertainty remains in the numerical results. Therefore, it is not possible to identify the best-performing mechanism. In the methane simulations, no mechanism shows an excellent agreement. Both AramcoMech 2.0 and HP-mech predict the ignition threshold correctly. But, again, this property is sensitive to the deposited energy. This highlights the need for accurate deposited energy measurements in this type of reactor. Still, the qualitative agreement with experimental data provides confidence in our methodology. A detailed flux analysis is performed to investigate key chemical pathways in the plasma-assisted oxidation of H_2 and CH_4. In the oxidation of H_2 identified pathways are very similar among the three different mechanisms. However, differences are present in the oxidation of CH_4, especially in the early stages of oxidation. The largest difference is present in the pathways involving the formation of CH_3OH below 700K. Consequently, measurements of methanol production in a $CH_4/O_2/Ar$ plasma below 700K would be valuable to obtain a deeper understanding of this early stage of low-temperature CH_4 oxidation.

In the oxidation of H_2, three different modes are identified, each prevalent in a different temperature range. For increasing temperature the ability of a $H_2/O_2/Ar$ mixture to self-sustain oxidation increases. Even at modest temperatures ($T \approx 800$K), plasma provides the initial radicals after which hydrogen oxidation chemistry takes over and completes the oxidation. Three different oxidation modes are identified for CH_4 as well. However, in CH_4 the ability of self-sustained oxidation below 1000K is not observed. As such, the oxidation of CH_4, in these diluted conditions ($X_{Ar} > 0.99$), requires a continuous supply of radicals. We conclude that this is an inherent limitation of CH_4, due to the chain-terminating nature of the low-temperature oxidation pathways. More specifically, the pathways involved in the conversion of CH_4 into CH_3OH or CH_2O below 1000K are chain-terminating. This implies that plasma can initiate combustion by providing initial radicals, but it can not induce ignition below the ignition temperature. As this seems to be an inherent limitation of the oxidation chemistry, not the plasma chemistry, this observation is likely to translate to non-diluted conditions and other bath gases. The only exception is the chemical heat release, which provides a positive feedback mechanism on the oxidation rate via the temperature.

Novelty and Significance

In this article, an extensive chemical flux analysis is performed on the plasma-assisted oxidation of hydrogen and methane. To this end, we introduce a thermodynamically consistent plasma mechanism, which is coupled to three combustion mechanisms. The chemical mechanisms are time-integrated with a 0D dielectric barrier discharge model. To validate our methodology and the mechanisms the results are compared to experimental measurements. The flux analysis reveals similarities among the mechanisms for the oxidation of hydrogen, but also differences in the case of methane. The main differences are found in the pathways involved in the production of methanol, providing targets for future experimental measurements. Most importantly, our analysis reveals that the inherent chain-terminating nature of low-temperature methane oxidation cannot be overcome by plasma. Evidence is provided that significant thermal activation is still required in the presence of plasma when using methane. In contrast to methane, when using hydrogen, chain-branching is observed during the low-temperature plasma-assisted oxidation.

Declaration of Competing Interest

The authors declare that they have no known competing financial interests or personal relationships that could have appeared to influence the work reported in this paper.

CRediT authorship contribution statement

T. Hazenberg: Conceptualization, Methodology, Software, Validation, Formal analysis, Investigation, Writing – original draft. **J. van Dijk:** Conceptualization, Writing – review & editing, Supervision, Funding acquisition. **J.A. van Oijen:** Conceptualization, Writing – review & editing, Supervision, Funding acquisition.

Acknowledgments

This work is part of the research program “Making plasma-assisted combustion efficient” with project number 16480, which is partly financed by the Dutch Research Council (NWO).

Supplementary material

Supplementary material associated with this article can be found, in the online version, at doi:10.1016/j.combustflame.2023.113037

References

[1] S.M. Starikovskaia, Plasma assisted ignition and combustion, J. Phys. D: Appl. Phys. 39 (16) (2006) R265–R299, doi:10.1088/0022-3727/39/16/R01.
[2] I.V. Adamovich, I. Choi, N. Jiang, J.-H. Kim, S. Keshav, W.R. Lempert, E. Mintusov, M. Nishihara, M. Samimy, M. Uddi, Plasma assisted ignition and high-speed flow control: non-thermal and thermal effects, Plasma Sources Sci. Technol. 18 (3) (2009) 034018, doi:10.1088/0963-0252/18/3/034018.
[3] A. Starikovskiy, N. Aleksandrov, Plasma-assisted ignition and combustion, Prog. Energy Combust. Sci. 39 (1) (2013) 61–110, doi:10.1016/j.pecs.2012.05.003.
[4] I.V. Adamovich, W.R. Lempert, Challenges in understanding and predictive model development of plasma-assisted combustion, Plasma Phys. Controlled Fusion 57 (1) (2014) 014001, doi:10.1088/0741-3335/57/1/014001.
[5] Y. Ju, W. Sun, Plasma assisted combustion: Dynamics and chemistry, Prog. Energy Combust. Sci. 48 (2015) 21–83, doi:10.1016/j.pecs.2014.12.002.
[6] Y. Ju, J.K. Lefkowitz, C.B. Reuter, S.H. Won, X. Yang, S. Yang, W. Sun, Z. Jiang, Q. Chen, Plasma assisted low temperature combustion, Plasma Chem. Plasma Process. 36 (1) (2015) 85–105, doi:10.1007/s11090-015-9657-2.
[7] N.A. Popov, Kinetics of plasma-assisted combustion: effect of non-equilibrium excitation on the ignition and oxidation of combustible mixtures, Plasma Sources Sci. Technol. 25 (4) (2016) 043002, doi:10.1088/0963-0252/25/4/043002.
[8] W. Sun, S.H. Won, T. Ombrello, C. Carter, Y. Ju, Direct ignition and s-curve transition by in situ nano-second pulsed discharge in methane/oxygen/helium counterflow flame, Proc. Combust. Inst. 34 (1) (2013) 847–855, doi:10.1016/j.proci.2012.06.104.
[9] W. Sun, S.H. Won, Y. Ju, In situ plasma activated low temperature chemistry and the s-curve transition in DME/oxygen/helium mixture, Combust. Flame 161 (8) (2014) 2054–2063, doi:10.1016/j.combustflame.2014.01.028.
[10] F. Tholin, D.A. Lacoste, A. Bourdon, Influence of fast-heating processes and o atom production by a nanosecond spark discharge on the ignition of a lean –air premixed flame, Combust. Flame 161 (5) (2014) 1235–1246, doi:10.1016/j.combustflame.2013.11.007.

[11] M.D.G. Evans, J.M. Bergthorson, S. Coulombe, Actuation of a lean-premixed flame by diffuse non-equilibrium nanosecond-pulsed plasma at atmospheric pressure, J. Appl. Phys. 122 (17) (2017) 173305, doi:10.1063/1.4995964.

[12] D.A. Lacoste, J.P. Moeck, W.L. Roberts, S.H. Chung, M.S. Cha, Analysis of the step responses of laminar premixed flames to forcing by non-thermal plasma, Proc. Combust. Inst. 36 (3) (2017) 4145–4153, doi:10.1016/j.proci.2016.06.178.

[13] J. Lambert, S. Coulombe, G. Bourque, J.M. Bergthorson, Investigation of the hydrodynamic effect of nanosecond repetitively pulsed discharges on a laminar stagnation flame, Proc. Combust. Inst. 38 (4) (2021) 6567–6574, doi:10.1016/j.proci.2020.06.166.

[14] M. Uddi, N. Jiang, I.V. Adamovich, W.R. Lempert, Nitric oxide density measurements in air and air/fuel nanosecond pulse discharges by laser induced fluorescence, J. Phys. D: Appl. Phys. 42 (7) (2009) 075205, doi:10.1088/0022-3727/42/7/075205.

[15] Z. Yin, A. Montello, C.D. Carter, W.R. Lempert, I.V. Adamovich, Measurements of temperature and hydroxyl radical generation/decay in lean fuel–air mixtures excited by a repetitively pulsed nanosecond discharge, Combust. Flame 160 (9) (2013) 1594–1608, doi:10.1016/j.combustflame.2013.03.015.

[16] J.K. Lefkowitz, P. Guo, A. Rousso, Y. Ju, Species and temperature measurements of methane oxidation in a nanosecond repetitively pulsed discharge, Philos. Trans. Royal Soc. A 373 (2048) (2015) 20140333, doi:10.1098/rsta.2014.0333.

[17] J.K. Lefkowitz, M. Uddi, B.C. Windom, G. Lou, Y. Ju, In situ species diagnostics and kinetic study of plasma activated ethylene dissociation and oxidation in a low temperature flow reactor, Proc. Combust. Inst. 35 (3) (2015) 3505–3512, doi:10.1016/j.proci.2014.08.001.

[18] N. Tsolas, J.G. Lee, R.A. Yetter, Flow reactor studies of non-equilibrium plasma-assisted oxidation of *n*-alkanes, Philos. Trans. Royal Soc. A 373 (2048) (2015) 20140344, doi:10.1098/rsta.2014.0344.

[19] N. Tsolas, K. Togai, Z. Yin, K. Frederickson, R.A. Yetter, W.R. Lempert, I.V. Adamovich, Plasma flow reactor studies of H2/O2/Ar kinetics, Combust. Flame 165 (2016) 144–153, doi:10.1016/j.combustflame.2015.11.021.

[20] C. Winters, Z. Eckert, Z. Yin, K. Frederickson, I.V. Adamovich, Measurements and kinetic modeling of atomic species in fuel-oxidizer mixtures excited by a repetitive nanosecond pulse discharge, J. Phys. D: Appl. Phys. 51 (1) (2017) 015202, doi:10.1088/1361-6463/aa9942.

[21] E.R. Jans, I.W. Jones, X. Yang, T.A. Miller, J.F. Stanton, I.V. Adamovich, Time-resolved measurements of HO2 radical in a heated plasma flow reactor, Combust. Flame 241 (2022) 112097, doi:10.1016/j.combustflame.2022.112097.

[22] R. Patel, J. van Oijen, N. Dam, S. Nijdam, Low-temperature filamentary plasma for ignition-stabilized combustion, Combust. Flame 247 (2023) 112501, doi:10.1016/j.combustflame.2022.112501.

[23] P. Koelman, S. Heijkers, S.T. Mousavi, W. Graef, D. Mihailova, T. Kozak, A. Bogaerts, J. van Dijk, A comprehensive chemical model for the splitting of CO in non-equilibrium plasmas, Plasma Processes Polym. 14 (4–5) (2016) 1600155, doi:10.1002/ppap.201600155.

[24] W. Wang, R. Snoeckx, X. Zhang, M.S. Cha, A. Bogaerts, Modeling plasma-based CO2 and CH4 conversion in mixtures with N2, O2, and H2O: The bigger plasma chemistry picture, J. Phys. Chem. C 122 (16) (2018) 8704–8723, doi:10.1021/acs.jpcc.7b10619.

[25] V. Guerra, A. Tejero-del Caz, C.D. Pintassilgo, L.L. Alves, Modelling N_2–O_2 plasmas: volume and surface kinetics, Plasma Sources Sci. Technol. 28 (7) (2019) 073001, doi:10.1088/1361-6595/ab252c.

[26] N. Popov, S. Starikovskaia, Relaxation of electronic excitation in nitrogen/oxygen and fuel/air mixtures: fast gas heating in plasma-assisted ignition and flame stabilization, Prog. Energy Combust. Sci. 91 (2022) 100928, doi:10.1016/j.pecs.2021.100928.

[27] A.C. DeFilippo, J.Y. Chen, Modeling plasma-assisted methane–air ignition using pre-calculated electron impact reaction rates, Combust. Flame 172 (2016) 38–48, doi:10.1016/j.combustflame.2016.07.005.

[28] X. Mao, Q. Chen, Effects of vibrational excitation on nanosecond discharge enhanced methane–air ignition, AIAA J. 56 (11) (2018) 4312–4320, doi:10.2514/1.j057304.

[29] L. Cheng, N. Barleon, B. Cuenot, O. Vermorel, A. Bourdon, Plasma assisted combustion of methane-air mixtures: Validation and reduction, Combust. Flame 240 (2022) 111990, doi:10.1016/j.combustflame.2022.111990.

[30] R. Snoeckx, D. Jun, B.J. Lee, M.S. Cha, Kinetic study of plasma assisted oxidation of H2 for an undiluted lean mixture, Combust. Flame 242 (2022) 112205, doi:10.1016/j.combustflame.2022.112205.

[31] R. Snoeckx, M.S. Cha, Kinetic study of plasma assisted oxidation of H2 for an undiluted rich mixture, Combust. Flame 250 (2023) 112638, doi:10.1016/j.combustflame.2023.112638.

[32] G.P. Smith, D.M. Golden, M. Frenklach, N.W. Moriarty, B. Eiteneer, M. Goldenberg, C.T. Bowman, R.K. Hanson, S. Song, W.C. Gardiner, V.V.L. Jr., Z. Qin, GRImech 3.0,

[33] A. Kéromnès, W.K. Metcalfe, K.A. Heufer, N. Donohoe, A.K. Das, C.-J. Sung, J. Herzler, C. Naumann, P. Griebel, O. Mathieu, M.C. Krejci, E.L. Petersen, W.J. Pitz, H.J. Curran, An experimental and detailed chemical kinetic modeling study of hydrogen and syngas mixture oxidation at elevated pressures, Combust. Flame 160 (6) (2013) 995–1011, doi:10.1016/j.combustflame.2013.01.001.

[34] W.K. Metcalfe, S.M. Burke, S.S. Ahmed, H.J. Curran, A hierarchical and comparative kinetic modeling study of C_1 - C_2 hydrocarbon and oxygenated fuels, Int. J. Chem. Kinet. 45 (10) (2013) 638–675, doi:10.1002/kin.20802.

[35] S.M. Burke, W. Metcalfe, O. Herbinet, F. Battin-Leclerc, F.M. Haas, J. Santner, F.L. Dryer, H.J. Curran, An experimental and modeling study of propene oxidation. part 1: Speciation measurements in jet-stirred and flow reactors, Combust. Flame 161 (11) (2014) 2765–2784, doi:10.1016/j.combustflame.2014.05.010.

[36] X. Shen, X. Yang, J. Santner, J. Sun, Y. Ju, Experimental and kinetic studies of acetylene flames at elevated pressures, Proc. Combust. Inst. 35 (1) (2015) 721–728, doi:10.1016/j.proci.2014.05.106.

[37] H. Zhao, J. Fu, F.M. Haas, Y. Ju, Effect of prompt dissociation of formyl radical on 1,3,5-trioxane and CH2O laminar flame speeds with CO2 dilution at elevated pressure, Combust. Flame 183 (2017) 253–260, doi:10.1016/j.combustflame.2017.05.005.

[38] M. Fischer, X. Jiang, A chemical kinetic modelling study of the combustion of CH4–CO–H2–CO2 fuel mixtures, Combust. Flame 167 (2016) 274–293, doi:10.1016/j.combustflame.2016.02.001.

[39] N. Zettervall, C. Fureby, E.J.K. Nilsson, Evaluation of chemical kinetic mechanisms for methane combustion: A review from a CFD perspective, Fuels 2 (2) (2021) 210–240, doi:10.3390/fuels2020013.

[40] X. Mao, H. Zhong, T. Zhang, A. Starikovskiy, Y. Ju, Modeling of the effects of non-equilibrium excitation and electrode geometry on H2/air ignition in a nanosecond plasma discharge, Combust. Flame 240 (2022) 112046, doi:10.1016/j.combustflame.2022.112046.

[41] N. Tsolas, R.A. Yetter, Kinetics of plasma assisted pyrolysis and oxidation of ethylene. Part 1: Plasma flow reactor experiments, Combust. Flame 176 (2017) 534–546, doi:10.1016/j.combustflame.2016.10.022.

[42] K. Togai, N. Tsolas, R.A. Yetter, Kinetics of plasma-assisted oxidation of methane, 54th AIAA Aerospace Sciences Meeting, 2016. 10.2514/6.2016-0192

[43] H. Zhong, M.N. Shneider, M.S. Mokrov, Y. Ju, Thermal-chemical instability of weakly ionized plasma in a reactive flow, J. Phys. D: Appl. Phys. 52 (48) (2019) 484001, doi:10.1088/1361-6463/ab3d69.

[44] H. Zhong, M.N. Shneider, M.S. Mokrov, Y. Ju, Thermal-chemical plasma instability in a reacting flow, AIAA Scitech 2020 Forum (2020), doi:10.2514/6.2020-1661.

[45] R. Snoeckx, R. Aerts, X. Tu, A. Bogaerts, Plasma-based dry reforming: A computational study ranging from the nanoseconds to seconds time scale, J. Phys. Chem. C 117 (10) (2013) 4957–4970, doi:10.1021/jp311912b.

[46] R. Snoeckx, M.S. Cha, Inevitable chemical effect of balance gas in low temperature plasma assisted combustion, Combust. Flame 225 (2021) 1–4, doi:10.1016/j.combustflame.2020.10.028.

[47] Z. Eckert, N. Tsolas, K. Togai, A. Chernukho, R.A. Yetter, I.V. Adamovich, Kinetics of plasma-assisted oxidation of highly diluted hydrocarbon mixtures excited by a repetitive nanosecond pulse discharge, J. Phys. D: Appl. Phys. 51 (37) (2018) 374002, doi:10.1088/1361-6463/aad2b1.

[48] T. Hazenberg, J.F.J. Janssen, J. van Dijk, J.A. van Oijen, Consistent thermodynamics for plasma-assisted combustion, Proc. Combust. Inst. (2022), doi:10.1016/j.proci.2022.07.075.

[49] K. Togai, N. Tsolas, R.A. Yetter, Kinetic modeling and sensitivity analysis of plasma-assisted oxidation in a H2/O2/Ar mixture, Combust. Flame 164 (2016) 239–249, doi:10.1016/j.combustflame.2015.11.020.

[50] A. Pipa, R. Brandenburg, The equivalent circuit approach for the electrical diagnostics of dielectric barrier discharges: The classical theory and recent developments, Atoms 7 (1) (2019) 14, doi:10.3390/atoms7010014.

[51] D.Z. Pai, G.D. Stancu, D.A. Lacoste, C.O. Laux, Nanosecond repetitively pulsed discharges in air at atmospheric pressure—the glow regime, Plasma Sources Sci. Technol. 18 (4) (2009) 045030, doi:10.1088/0963-0252/18/4/045030.

[52] D.L. Rusterholtz, D.A. Lacoste, G.D. Stancu, D.Z. Pai, C.O. Laux, Ultrafast heating and oxygen dissociation in atmospheric pressure air by nanosecond repetitively pulsed discharges, J. Phys. D: Appl. Phys. 46 (46) (2013) 464010, doi:10.1088/0022-3727/46/46/464010.

[53] A.C. Hindmarsh, P.N. Brown, K.E. Grant, S.L. Lee, R. Serban, D.E. Shumaker, C.S. Woodward, SUNDIALS, ACM Trans. Math. Softw. 31 (3) (2005) 363–396, doi:10.1145/1089014.1089020.

[54] D.J. Gardner, D.R. Reynolds, C.S. Woodward, C.J. Balos, Enabling new flexibility in the SUNDIALS suite of nonlinear and differential/algebraic equation solvers, ACM Trans. Math. Softw. 48 (3) (2022) 1–24, doi:10.1145/3539801.

[55] Ansys, ANSYS chemkin theory manual 17.0 (15151), reaction design, san diego, 2015.

[56] G.J.M. Hagelaar, L.C. Pitchford, Solving the boltzmann equation to obtain electron transport coefficients and rate coefficients for fluid models, Plasma Sources Sci. Technol. 14 (4) (2005) 722–733, doi:10.1088/0963-0252/14/4/011.

[57] N. Tsolas, Flow Reactor Studies of Non-Equilibrium Plasma-Assisted Combustion Kinetics, 2015 Ph.D. thesis. Ph.D. thesis, Pennsylvania State University

[58] S. Pancheshnyi, S. Biagi, M.C. Bordage, G.J.M. Hagelaar, W.L. Morgan, A.V. Phelps, L.C. Pitchford, The LXCat project: Electron scattering cross sections and swarm parameters for low temperature plasma modeling, Chem. Phys. 398 (2012) 148–153, doi:10.1016/j.chemphys.2011.04.020.

[59] L.L. Alves, The IST-lisbon database on LXCat, J. Phys: Conf. Ser. 565 (2022). 2014

[60] D. Bouwman, A. Martinez, B.J. Braams, U. Ebert, Neutral dissociation of methane by electron impact and a complete and consistent cross section set, Plasma Sources Sci. Technol. 30 (7) (2021) 075012, doi:10.1088/1361-6595/ac0b2b.

[61] M.-Y. Song, J.-S. Yoon, H. Cho, Y. Itikawa, G.P. Karwasz, V. Kokoouline, Y. Nakamura, J. Tennyson, Cross sections for electron collisions with methane, J. Phys. Chem. Ref. Data 44 (2) (2015) 023101, doi:10.1063/1.4918630.

[62] Morgan database, 2022, https://www.lxcat.net/Morgan.

[63] I.V. Adamovich, M. Nishihara, I. Choi, M. Uddi, W.R. Lempert, Energy coupling to the plasma in repetitive nanosecond pulse discharges, Phys. Plasmas 16 (11) (2009) 113505, doi:10.1063/1.3264740.

[64] N. Tsolas, R.A. Yetter, I.V. Adamovich, Kinetics of plasma assisted pyrolysis and oxidation of ethylene. Part 2: Kinetic modeling studies, Combust. Flame 176 (2017) 462–478, doi:10.1016/j.combustflame.2016.10.023.
[65] Y. Li, C.-W. Zhou, K.P. Somers, K. Zhang, H.J. Curran, The oxidation of 2-butene: A high pressure ignition delay, kinetic modeling study and reactivity comparison with isobutene and 1-butene, Proc. Combust. Inst. 36 (1) (2017) 403–411, doi:10.1016/j.proci.2016.05.052.
[66] S.H. Mousavipour, Z. Homayoon, Multichannel RRKM-TST and CVT rate constant calculations for reactions of CH2OH or CH3O with HO2, J. Phys. Chem. A 115 (15) (2011) 3291–3300, doi:10.1021/jp112081r.